OBSERVATION OF BERRY'S PHASE IN A TRANSMON QUBIT

Master's Thesis in Physics
Presented by Simon Berger
Supervised by Dr. Stefan Filipp
Handed in to Prof. Dr. Andreas Wallraff,
Laboratory for Solid State Physics, ETH Zurich

Zurich, February 15, 2010

And then he lifted up his Throat
And squandered such a Note,
A Universe that overheard
Is stricken by it yet –

Emily Dickinson

Abstract

Quantum computation offers rivetting prospects that are out of reach for classical computation, but the path leading to a fully-fledged quantum computer is arduous. It presents the scientific community with copious challenges, notably finding a practicable way to manipulate and store the quantum bits, or qubits. Circuit quantum electrodynamics, the architecture used in this thesis, is a promising approach to superconducting quantum computation. The qubit is implemented as a superconducting circuit, called transmon, connected to a transmission line resonator which allows both qubit manipulation and readout.

Quantum algorithms consist of operations performed on the phase of the qubit wavefunction. The wavefunction can acquire two kinds of phases, dynamic and geometric. While the dynamic phase is dictated by the Hamiltonian which governs qubit evolution, the geometric phase can be viewed as a 'memory' of the evolution the system has undergone. The aim of this thesis is to measure a particular kind of geometric phase, termed Berry's phase. This is achieved by precise manipulations of the qubit using microwave photons sent into the resonator.

After a succinct outline of the theoretical framework underlying this thesis—cavity quantum electrodynamics and the transmon—geometrical phases are introduced. We show how this concept arises in quantum mechanics and how a qubit can be brought to accumulate such a phase. The qubit is realised as the two lowest energy levels of the transmon. We then present a description of the fabrication of the qubit, of the cryogenic setup it is placed in, and of the microwave equipment used to control it and read it out. The foundations of the dispersive readout scheme are also explained.

The experimental part of this thesis details the extent of qubit control that is requisite to measure Berry's phase, including precisely determining the transition frequency and inducing high-visibility Rabi flopping. We show how we achieved enhanced qubit control and how this permitted to measure Berry phases which are in good agreement with theoretical predictions. In particular, we improved the accuracy of the microwave pulses used to induce Rabi flopping. The influence of the higher levels of the transmon, which are not explicitely used during a geometric phase measurement, was also taken into account. Our results demonstrate the potential use of geometric phases in quantum computation.

Contents

List of Figures

1 Introduction

In 1965, Gordon Moore proposed what has become known as Moore's law: the computer power available at constant cost doubles every other year. Technological advances have permitted the production of smaller and smaller components of computer hardware and Moore's law has held true ever since. However, pursuing this approach, we are bound to come up against a brick wall. When the components of computer hardware are so minute that quantum effects cannot be disregarded any longer, we can either panic—or embrace the wealth of possibilities quantum physics offers. Then again, it is sensible to explore alternatives to miniaturisation before quantum mechanical effects impede the development of computers. This feat, exploring the realm of quantum computation, was most conspicuously spurred on by Shor's factoring algorithm [1] and Grover's search algorithm [2], both discovered in the 1990s. Although it is unknown whether quantum computation will save Moore's law, it is per se worth to be explored.

Building a quantum computer is a daunting task. However, since the early days of quantum computation, a number of exploits have been achieved in the variety of implementations of qubits—ion traps, quantum dots and superconducting qubits, to name but a few [3]. As of now, it is possible to address a single qubit in a row of eight qubits [4], or to use light to convey information from one qubit to another [5]. A description of superconducting qubits, followed by a discussion of some common time domain measurments can be found in Ref. [6].

Ultimately, a quantum computer should be able to perform quantum algorithms or simulate quantum-mechanical systems. Quantum algorithms rely on operations performed on the building blocks of quantum computers, the qubits. In the architecture used in this thesis, called circuit QED [7], the qubit is realised as a superconducting structure called transmon [8]. It is accessible to the experimenter via a one-dimensional resonator that effectively shields the qubit from the environment. Microwave signals sent into this resonator allow accurate qubit control. The dispersive shift of the resonator frequency, which depends on the qubit state, permits to read out the qubit.

Decoherence is the interaction of an open quantum system with its environment. This process slows down the development of quantum information processing and would make it infeasible were it not for error correction (see, for example, Ref. [9]). Qubits can acquire two kinds of phases: geometric and dynamic [10]. Geometric phases (unlike dynamic phases) are independent of energy and time and it has been proposed [11] that they are more robust against decoherence. The aim of the so-called holonomic quantum computation [12] is to perform qubit operations relying on geometric phases only. Berry's phase is a particular kind of geometric phase arising when the state of the qubit is modified slowly (with respect to its intrinsic timescale) and when, after its evolution, the qubit is returned to its original state [13]. What makes its observation worthwhile is not only the potential use as a quantum logic gate in circuit

QED, but also the fact that a mesoscopic system, the transmon, assumes the role of an artificially generated spin-1/2 particle and acquires a phase which is intrinsically of quantal origin.

2 Theory on qubits, circuit QED and geometric phases

2.1 Qubits

A classical bit is the fundamental building block of classical information theory and classical computation. It assumes either the value 0 or the value 1. The basis of quantum computation is the quantum bit, or qubit.

Mathematically, the wavefunction $|\psi\rangle$ of a qubit is described by a unit vector in the vector space $\mathbb{C}$ equipped with the basis $(|0\rangle, |1\rangle)$:

$$|\psi\rangle = \alpha|0\rangle + \beta|1\rangle, \quad |\alpha|^2 + |\beta|^2 = 1. \tag{2.1}$$

In contrast to the classical bit, a qubit is a linear combination of the basis vectors. Still, when measuring its state, there are only two possible measurement outcomes: $|0\rangle$ and $|1\rangle$. The probability of observing outcome $|0\rangle$ (respectively $|1\rangle$) is $|\alpha|^2$ (respectively $|\beta|^2$). The normalisation of the wavefunction $|\psi\rangle$ stems from the fact that the probability of observing the qubit in either state must add up to 1. Note that the measurement causes the wavefunction to collapse. After the measurement, the qubit is either $|0\rangle$ or $|1\rangle$.

Since reading out a qubit invariably gives $|0\rangle$ or $|1\rangle$, what is, then, the advantage of qubits over classical bits? One advantage is that superposition states can be used *during* computation. Another advantage lies in the way two (or more) qubits are assembled to form a product system. The joint wavefunction $|\Psi\rangle$ of two qubits described by the wavefunctions $|\psi\rangle$ and $|\psi'\rangle$ is the tensor product of the single qubit wavefunction:

$$|\Psi\rangle = |\psi\rangle \otimes |\psi'\rangle \in \mathbb{C} \otimes \mathbb{C} \cong \mathbb{C}^2.$$

The tensor product gives rise to intriguing properties that cannot be emulated using two classical bits, most notably entanglement. A measurement on $|\psi\rangle$ will cause the wave function $|\Psi\rangle$ to collapse; not only will the state of $|\psi\rangle$ be determined but also the state of $|\psi'\rangle$, even before any information has flowed between the qubits.

Physically, qubits can be implemented in a variety of ways. One can use either a spin-1/2 system represent the basis vectors, the spin-up (spin-down) state corresponding to $|1\rangle$ ($|0\rangle$) or employ a many-level-system restricted to two of its levels. The qubit used within this thesis, the transmon, is of the latter kind. The reader will find some details on this matter and its implications concerning qubit control in section 2.4.

Bloch sphere.— A useful way to represent a single qubit is the Bloch sphere (named after Swiss scientist Felix Bloch). It was initially designed for spin analysis in nuclear magnetic resonance.

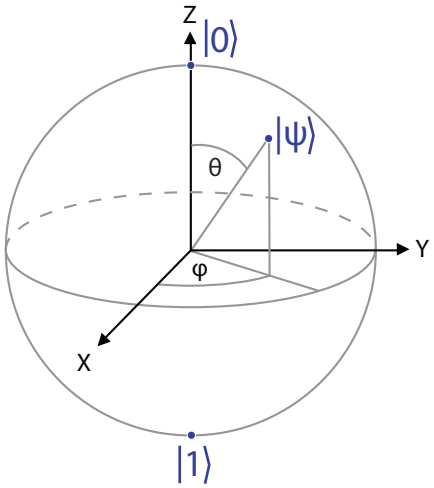

Figure 2.1: The wavefunction $|\psi\rangle$ of a qubit represented on the Bloch sphere.

We rewrite (2.1) without loss of generality as

$$|\psi(\vartheta,\varphi)\rangle = e^{i\gamma}\left(\cos\left(\frac{\vartheta}{2}\right)|0\rangle + e^{i\varphi}\sin\left(\frac{\vartheta}{2}\right)|1\rangle\right),$$

where $\gamma, \vartheta, \varphi \in \mathbb{R}$. The overall phase factor $e^{i\gamma}$ is irrelevant because it cannot be measured. (Note that in case where the qubit has three levels, this phase factor becomes relevant.) Moreover, it is possible to adjust the phase of $|\psi\rangle$ so that the coefficient of $|0\rangle$ is real. Consider the operator $\mathbf{r}(\vartheta,\varphi)\cdot\boldsymbol{\sigma}$, where $\mathbf{r}(\vartheta,\varphi) \in \mathbb{R}^3$ is called the Bloch vector,

$$\mathbf{r}(\vartheta,\varphi) = (r_x, r_y, r_z) = (\sin\vartheta\cos\varphi, \sin\vartheta\sin\varphi, \cos\vartheta) \tag{2.2}$$

and $\boldsymbol{\sigma}$ are the Pauli matrices,

$$\boldsymbol{\sigma} = \left(\sigma_x, \sigma_y, \sigma_z\right) = \left(\begin{pmatrix} 0 & 1 \\ 1 & 0 \end{pmatrix}, \begin{pmatrix} 0 & -i \\ i & 0 \end{pmatrix}, \begin{pmatrix} 1 & 0 \\ 0 & -1 \end{pmatrix}\right).$$

A straightforward computation shows that $|\psi(\vartheta,\varphi)\rangle$ is an eigenstate of $\mathbf{r}(\vartheta,\varphi)\cdot\boldsymbol{\sigma}$ with eigenvalue 1. So there is a natural bijection [3] between a vector $\mathbf{r}(\vartheta,\varphi)$ to the state $|\psi(\vartheta,\varphi)\rangle$, provided $0 \le \vartheta \le \pi$ and $0 \le \varphi < 2\pi$. The collection of vectors $\mathbf{r}(\vartheta,\varphi)$ is precisely the unit sphere, which, in this context, is called the Bloch sphere, see Fig. 2.1 These vectors describe the so-called pure states and can be written as a wavefunction $|\psi\rangle$ as in eqn. (2.1). What about the states in the interior of the Bloch sphere? Their state vector is of the form

$$\mathbf{r}(\vartheta,\varphi) = (\rho\sin\vartheta\cos\varphi, \rho\sin\vartheta\sin\varphi, \rho\cos\vartheta), \tag{2.3}$$

for some $\rho \in [0,1[$. These states are called mixed states. They cannot be described by a wavefunction $|\psi\rangle$. We need density matrices in order to discuss them.

Density matrices.— The density matrix associated with a pure state $|\psi\rangle$ is the 2×2-matrix with complex entries $\rho = |\psi\rangle\langle\psi|$. Mixed states are also described by such matrices, but there is no wavefunction $|\psi\rangle$ such that $\rho = |\psi\rangle\langle\psi|$. The density matrices associated with physical (pure or mixed) qubit states must fulfil two properties. Namely, their trace must be equal to one, $\operatorname{tr}\rho = 1$, and they must be positive semi-definite. We may equip the space of density matrices with the Hilbert-Schmidt inner product $(\cdot,\cdot)$ [14],

$$(\rho_1, \rho_2) = \operatorname{tr}(\rho_1^\dagger \rho_2).$$

Because the set $\{\mathrm{id}_2/\sqrt{2}, \sigma_x/\sqrt{2}, \sigma_y/\sqrt{2}, \sigma_z/\sqrt{2}\}$, where id_2 is the 2×2 identity matrix, forms an orthonormal set with respect to the Hilbert-Schmidt inner product, any density matrix ρ may be expanded as

$$\rho = \frac{1}{2}\left(\operatorname{tr}(\mathrm{id}_2\rho)\mathrm{id}_2 + \operatorname{tr}(\sigma_x\rho)\sigma_x + \operatorname{tr}(\sigma_y\rho)\sigma_y + \operatorname{tr}(\sigma_z\rho)\sigma_z\right). \tag{2.4}$$

The above can be identified with eqn. 2.3, provided $\operatorname{tr}(\sigma_i\rho) = \mathbf{r}(\vartheta,\varphi)_i$ for $i = x, y, z$. This is indeed the case, because expressions like $\operatorname{tr}(\sigma_x\rho)$ are interpreted to be the expectation value $\langle\sigma_x\rangle_\rho \equiv \langle\sigma_x\rangle$ of spin projection operator σ_x with respect to the state ρ. For this reason, we also write

$$\mathbf{r} = (r_x, r_y, r_z) = (\langle\sigma_x\rangle, \langle\sigma_y\rangle, \langle\sigma_z\rangle).$$

2.2 Cavity quantum electrodynamics

Cavity Quantum Electrodynamics (cavity QED) is a subfield of quantum optics which emerged in the 1970s. After the so-called weak-coupling-regime age, during which e.g. spontaneous emission enhancement and inhibited spontaneous emission were observed, the strong-coupling-regime age came about. In 1992, the first quantum Rabi oscillations were observed and single atom masers were realised. A brief account of the history of cavity QED can be found in Refs. [15] or [16]. In cavity QED experiments, an electromagnetic field, optical or microwave, is confined in a cavity with highly reflecting walls. Atoms are sent through the cavity one by one and interact with the photons stored in it. In optical cavity QED, the cavity is driven with a laser while the atoms fall through it. The coupling between the atom and the quantised electromagnetic modes of the cavity causes detectable changes in the cavity transmission. The spontaneous emission in transverse directions can also be monitored. In microwave cavity QED, photons are coupled to transitions in highly excited Rydberg atoms via high-Q superconducting resonators [7].

Currently a variety of physical implementations of qubits are being studied [17], e.g. liquid-state or solid-state nuclear magnetic resonance, trapped ions, quantum dots and superconducting circuits. A number of prerequisites for a viable quantum computer were formulated by David DiVincenzo in his seminal paper [18]. They include for instance the ability to initialise the qubits in a well-defined state or the possibility to manipulate the qubits at will or a sufficient shielding of the qubits from the environment. It has been argued that systems involving a few tens of qubits will first be realised in trapped ion systems, but that superconducting qubits are a strong contender [19].

Jaynes-Cummings Hamiltonian

The interaction between the atom and the cavity can be idealised as interaction between a two-level-system and a quantum harmonic oscillator. This system is described by the Jaynes-Cummings-Hamiltonian [7], which was introduced by Jaynes and Cummings [20] in 1963 to study the coupling of matter to electromagnetic fields. This Hamiltonian reads

$$H = \hbar\omega_r \left(a^\dagger a + \frac{1}{2}\right) + \frac{1}{2}\hbar\omega_a \sigma_z + g\hbar(a^\dagger \sigma_- + a\sigma_+) + H_\kappa + H_\gamma, \tag{2.5}$$

where $\sigma_\pm = \sigma_x \pm \mathrm{i}\sigma_y$ are the usual ladder operators. The first term of this Hamiltonian is the contribution from the quantum harmonic oscillator; ω_r is the resonator frequency and $a^\dagger a$ is the photon number operator, $a^\dagger a|n\rangle = n|n\rangle$. The second term of H is the contribution from the spin eigenstate of two-level-system; ω_a is the transition frequency of the two-level-system from ground to excited state and σ_z measures the spin eigenstate in z-direction. The third term expresses the coupling of coupling strength g between atom and cavity. The contribution proportional to $a^\dagger\sigma_-$ corresponds to the annihilation of a cavity photon combined with a downward transition of the atom, whereas the contribution proportional to $a\sigma_+$ corresponds to the creation of a cavity photon combined with an upward transition of the atom. The ultimate and penultimate terms of H express dissipative losses. H_κ is the coupling of the photons to the environment, its strength is determined by the ratio $\kappa = \omega_r/Q$ of the resonator frequency to the quality factor of the cavity. The quantity κ is called the photon decay rate. H_γ is the coupling of the two-level-system to modes other than the resonator mode; γ is the decay rate of the excited state into these channels.

We distinguish between two regimes: the weak coupling regime and the strong coupling regime. In the strong coupling regime, in which $g \gg \max\{\kappa, \gamma\}$, the interaction strength between cavity and two-level-system permits free energy exchange in processes such as vacuum Rabi oscillations, where the two-level-system repeatedly absorbs and emits a photon. In the context of circuit QED, vacuum Rabi oscillations were observed in Ref. [21]. In the weak coupling regime, on the other hand, this energy exchange is impossible.

The Jaynes-Cummings Hamiltonian may be generalised [8] to a multi-level-system by supplementing the contributions from the higher level transitions and the higher level atom-cavity coupling to eqn. (2.5):

$$H = \hbar\omega_r \left(a^\dagger a + \frac{1}{2}\right) + \sum_i \hbar\omega_{gi}|i\rangle\langle i| + \sum_{i,j} \hbar g_{ij}|i\rangle\langle j|(a^\dagger + a). \tag{2.6}$$

The labels i and j run through the energy levels of the atom, $i = g, e, f, h$ etc. The symbol ω_{gi} denotes the frequency from the ground level to the ith level and g_{ij} denote the coupling strength of the cavity to the transition from level j to level i. If the coupling strengths to higher levels are sufficiently small, or if care is taken not to excite higher levels, the corresponding terms can be discarded, and from (2.6) one recovers (2.5). The coupling strengths become small when the transitions are driven off-resonantly or in the dispersive limit.

Dispersive limit

The dispersive limit is attained when the the detunings between the cavity and the energy levels of the artificial atom are large, so when in particular the condition $|\omega_{ge} - \omega_r| \gg g_{01}$ is satisfied. Then, the Hamiltonian for the lowest two levels can be cast into the form [7]

$$H = \left(\frac{1}{2}\hbar\omega_a' + \hbar\chi a^\dagger a\right)\sigma_z + \hbar\omega_r' a^\dagger a. \tag{2.7}$$

This is the dispersive Jaynes-Cummings Hamiltonian. The frequencies ω_a' and ω_r' are renormalised (here, dispersively shifted) counterparts of ω_a and ω_r. In the above equation, the AC-Stark shift [22] becomes apparent: the transition frequency ω_a' is shifted by the amount 2χ for every photon trapped inside the cavity. The dispersive shift χ depends on the coupling strengths g_{ij} and on the transition frequencies ω_{gi} of the lowest two levels. As may be expected, the Hamiltonian (2.5) describing the interaction of radiation with a two-level-system can also be cast in a form similar to (2.7). The dispersive regime is of fundamental importance for the readout procedure, described in section 3.3.

2.3 Towards the transmon

Superconducting qubits can be based either on phase, charge or flux. The transmon is a development of the archetypal charge qubit, the Cooper pair box. In the following, we present some aspects of the theory behind the transmon, describing what physics its functionality relies upon and outlining the course of its development.

Josephson junctions

A Josephson junction is made of two superconducting electrodes separated by a thin insulating layer. The electrical circuit representation is shown in Fig. 2.2. Each electrode can be described by condensate wavefunctions

$$\Psi_k = \Psi_0 e^{i\vartheta_k}$$

with phase difference $\varphi = \vartheta_1 - \vartheta_2$. If the charges on the electrodes are $\pm Q$, the number of Cooper pairs is $n = -Q/2e$, where $-e$ is the electrical charge of the electron. The electrical charge Q and the phase φ obey the Josephson equations [23]

$$\begin{aligned} \dot{Q} &= I_\mathrm{J} - I_\mathrm{ext}, \\ \dot{\varphi} &= -2eV/\hbar, \end{aligned}$$

where $I_\mathrm{J} = I_\mathrm{c}\sin\varphi$ is the Josephson current and I_c is the critical current, the maximal current a junction can support. I_ext is an external current source and $V = Q/C_\mathrm{J}$ is the ratio of the charge to the junction capacitance C_J. From those equations, one derives $\ddot{\varphi} = \frac{2e}{\hbar C_\mathrm{J}}(I_\mathrm{J} - I_\mathrm{ext})$. This equation is the equation of motion $\frac{\partial}{\partial\varphi}L - \frac{\mathrm{d}}{\mathrm{d}t}\frac{\partial}{\partial\dot{\varphi}} = 0$ of the Lagrangian

$$L = \frac{1}{2}\frac{C_\mathrm{J}\hbar^2}{4e^2}\dot{\varphi}^2 + E_\mathrm{J}\cos\varphi + \frac{I_\mathrm{ext}\hbar}{2e},$$

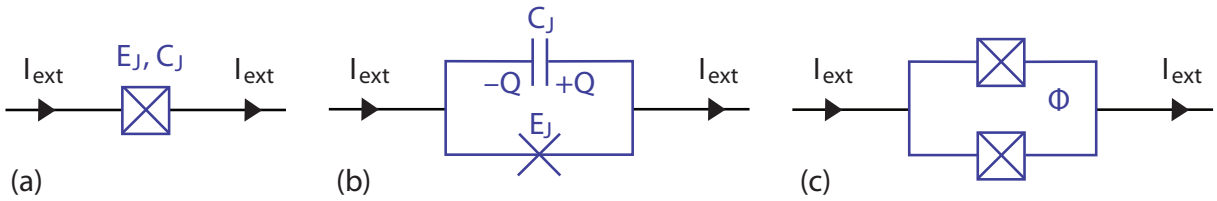

Figure 2.2: **(a)** The electric circuit diagram of a Josephson junction with Josephson energy E_J and capacitance C_J. **(b)** A more detailed model of the Josephson junction. The cross marks an ideal junction. The architecture of the junction, a dielectric layer sandwiched between conductors, gives rise to the capacitance C_J. **(c)** The electric circuit diagram of a SQUID. Graphics adapted from [3].

where

$$E_J = I_c \hbar / 2e \tag{2.8}$$

is the Josephson energy. One major drawback becomes apparent: E_J cannot be tuned *in situ*, it is determined by the geometry of the device, fixed at fabrication.

However, there is a device behaving like a Josephson junction with tunable Josephson energy: the so-called SQUID, short for superconducting quantum interference device. It consists of two Josephson junctions connected by two superconducting wires, cf. Fig. 2.2. Its Josephson energy is a function of the flux of the magnetic field Φ flowing through the loop [3],

$$E_J(\Phi) = E_J \cos \frac{\pi \Phi}{\Phi_0},$$

where $\Phi_0 = h/2e$ is the magnetic flux quantum. The relevant degree of freedom of the SQUID is the flux threading the loop. It is operated in the regime $E_J \gg E_C$.

The Cooper pair box

The simplest version of a qubit based on Josephson junctions is the Cooper pair box CPB. Consider a capacitor with capacitance C_g, biased by a gate voltage V_g, connected to a Josephson junction, as depicted in Fig. 2.3. The CPB consists of one of the electrodes of the capacitor with capacitance C_g, the connection between capacitor and Josephson junction, and one of the electrodes of the Josephson junction, as shown in Fig. 2.3. The part between the the capacitor and the junction is called the island.

Charge Basis.— In order to find the (quantised) Hamiltonian of the CPB, one applies a Legendre transform to the Lagrangian to find the Hamiltonian and imposes canonical commutation relations. The Lagrangian of the system is [3]

$$L = \frac{1}{2} C_J V_J^2 + \frac{1}{2} C_g (V_g - V_J)^2 + E_J \cos \varphi,$$

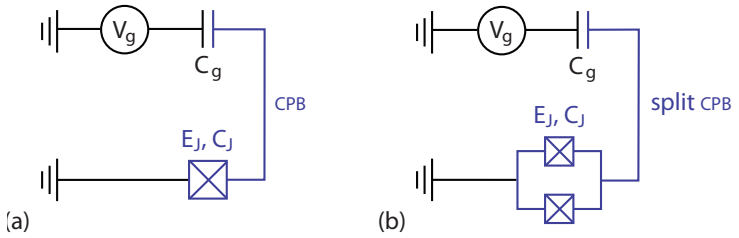

Figure 2.3: Circuit diagram of a charge qubit based on a CPB, (a) and a split CPB, (b). The additional Josephson junction in the split CPB permits to tune E_J. Graphics adapted from [3].

where $V_J = -\hbar\dot{\varphi}/2e$ is the voltage across the junction. The Lagrangian can be cast into the form

$$L = \left(\frac{\hbar}{2e}\right)^2 \frac{1}{2}(C_J + C_g)\dot{\varphi}^2 + E_J \cos\varphi + \frac{\hbar}{2e} C_g V_g \dot{\varphi}$$

if one neglects a constant term (of no importance when quantising). The total charge Q in the island is $Q = Q_J - Q_g = -2ep/\hbar = -2en$, where $p = \frac{d}{d\dot{\varphi}} L = \hbar n$ is the canonically conjugate momentum to φ. The Hamiltonian is

$$H = p\varphi - L = 4E_C(n - n_g)^2 - E_J \cos\varphi, \tag{2.9}$$

where $n_g = C_g V_g/2$ is the gate charge and $E_C = (2e)^2/2(C_g + C_J)$ is the charge energy. Imposing the canonical commutation relation $[\varphi, n] = i$ (and thus $\varphi = i\frac{d}{dn}$), the eigenstates $|n\rangle$ of the number operator n obey $e^{\pm i\varphi}|n\rangle = e^{\mp \frac{d}{dN}}|n\rangle = |n \pm 1\rangle$. Using this and the completeness relation for n, the above Hamiltonian can be written as

$$H = \sum_{n\in\mathbb{Z}} \left(\frac{1}{2} E_C (n - n_g)^2 |n\rangle\langle n| - \frac{1}{2} E_J (|n\rangle\langle n+1| + |n+1\rangle\langle n|) \right). \tag{2.10}$$

This is the Hamiltonian of CPB in the charge basis. The first term in the sum represents the electrostatic contribution, whereas the second term, the dynamical contribution, represents the tunnelling of Cooper pairs on and off the island. The above equation provides us with an intuitive understanding of the quantities E_J and E_C. Half the Coulomb energy, $E_C/2$, is the energy required to add a Cooper pair onto a charge neutral island. [3]. The Josephson energy E_J is the potential energy stored in the junction.

In the so-called charge regime, meaning $E_C \gg E_J$, and if n_g is tuned to be near a half-integer value of n, the states $|n\rangle$ and $|n+1\rangle$ have almost degenerate energies [3] and the other states can be ignored. Writing

$$|n\rangle = \begin{pmatrix} 1 \\ 0 \end{pmatrix}, \quad |n+1\rangle = \begin{pmatrix} 0 \\ 1 \end{pmatrix},$$

and discarding all terms involving other numbers than n and $n+1$, the Hamiltonian reduces to

$$H = -\frac{1}{2} E_J \begin{pmatrix} 0 & 1 \\ 1 & 0 \end{pmatrix} + 4E_C \begin{pmatrix} n_g^2 & 0 \\ 0 & 1 - 2n_g + n_g^2 \end{pmatrix} = -\frac{1}{2} B_x \sigma_x - \frac{1}{2} B_z \sigma_z. \tag{2.11}$$

In the above, where we defined $B_x = E_J$ and $B_z = 4E_C(1 - 2n_g)$, the last equality follows from dropping an irrelevant constant term (energy shift) proportional to the unit matrix. Note that H looks like the Hamiltonian of a spin-1/2 particle in a pseudo-magnetic field with components B_x and B_z. H has eigenvalues $\pm\frac{1}{2}\sqrt{B_x^2 + B_z^2}$. The corresponding eigenvectors are

$$|\uparrow\rangle = \cos\left(\frac{\vartheta}{2}\right)|0\rangle + \sin\left(\frac{\vartheta}{2}\right)|1\rangle \quad \text{and} \quad |\downarrow\rangle = -\sin\left(\frac{\vartheta}{2}\right)|0\rangle + \cos\left(\frac{\vartheta}{2}\right)|1\rangle,$$

where $\vartheta = \arctan B_x/B_z(N_g)$ is the mixing angle. The states $|\downarrow\rangle$ and $|\uparrow\rangle$ are the ground, respectively excited, eigenstates of the CPB. The energy splitting between the eigenstates is $\hbar\omega_a = \sqrt{B_x^2 + B_z^2}$.

Phase basis.— In order to solve the Hamiltonian (2.10) analytically, we swap the number n for its canonically conjugate variable φ. The Hamiltonian can then be solved in terms of the Mathieu functions [8]. To obtain H in the phase basis, one makes use of the relations

$$n = i\frac{\mathrm{d}}{\mathrm{d}\varphi}, \quad n\mathrm{e}^{\mathrm{i}\varphi} = \mathrm{e}^{\mathrm{i}\varphi(n+1)}$$

where the basis vectors can be expressed in terms of each other as

$$\sum_{n\in\mathbb{Z}} \mathrm{e}^{\mathrm{i}\varphi n}|n\rangle \quad \text{and} \quad |\varphi\rangle = \int_0^{2\pi} \mathrm{d}\varphi\, \mathrm{e}^{-\mathrm{i}\varphi n}|\varphi\rangle.$$

Then, one finds

$$H = 4E_C\left(\mathrm{i}\frac{\partial}{\partial\varphi} - \frac{n_g}{2}\right)^2 |\varphi\rangle\langle\varphi| - \frac{1}{2}E_J(\mathrm{e}^{\mathrm{i}\varphi} + \mathrm{e}^{-\mathrm{i}\varphi})|\varphi\rangle\langle\varphi|.$$

The solutions of the Hamiltonian are plotted in Fig. 2.4. In the limit $E_J/E_C \to 0$, the shape of the spectrum can be read off eqn. (2.10). Then, for each fixed n, the energy as a function of the gate charge n_g is a parabola centred at $n_g = n$.

The split Cooper pair box

Although the CPB has a tunable parameter, namely the gate charge n_g, it is a significant drawback that the Josephson energy E_J cannot be modified. Aspiring toward further control over the CPB, a device with tunable Josephson energy was created, the so-called split CPB. In essence, it consists of a CPB equipped with an additional Josephson junction, as can be seen from its effective circuit representation shown in Fig. 2.3. It can be shown [3] that the Josephson energy of the split CPB is

$$E_J(\Phi) = E_J \cos\left(\frac{\pi\Phi}{\Phi_0}\right),$$

where E_J is the Josephson energy of the CPB as defined in eqn. (2.8). This holds only if both Josephson junctions have the same Josephson energy, $E_J/2$.The Hamiltonian of the split CPB is identical with the Hamiltonian of the CPB, eqn. (2.11), with the exception that the coefficient B_x now depends on the flux, $B_x = B_x(\Phi) = E_J \cos(\pi\Phi/\Phi_0)$.

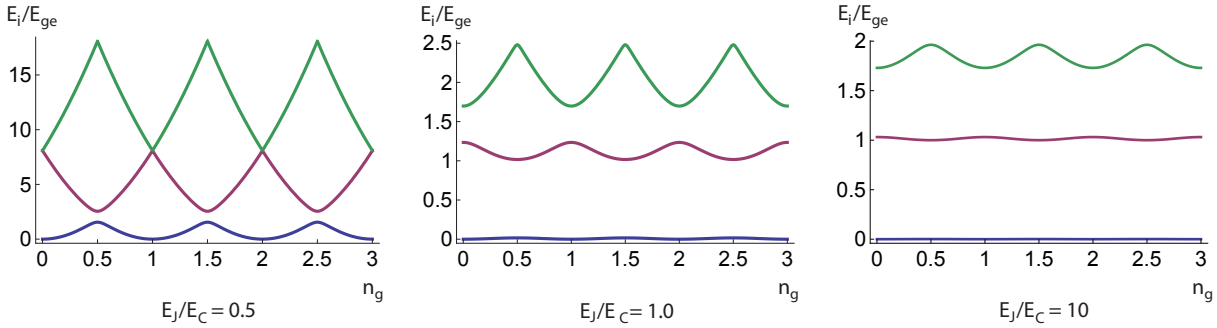

Figure 2.4: Energy levels E_{gi} of the CPB as a function of the gate charge n_g for various ratios E_J/E_C. The three lowest energy levels $i = e, f, h$ are shown. The energy levels are normalised with respect to the lowest transition E_{ge} (measured at the sweet spot) and are offset in such a way that the bottom of the lowest energy level is at zero. In the transmon regime (rightmost figure), the transition energy between ground and first excited state is approximately $\hbar\omega_a = \sqrt{8E_JE_C}$.

Considering the energy levels of the CPB plotted in 2.4, the presence of charge dispersion, that is, variation of the transition energy as a function of the gate charge n_g, is manifest. Whereas charge dispersion is comparatively low around the so-called sweet spot ($n_g = 0.5$), it increases away from it. It is desirable to operate the qubit at the sweet-spot since this has been demonstrated to increase dephasing time [24]. At the sweet spot, the linear dependence on charge noise is eliminated [8]. However, due to slow drifts in the gate charge, it needs to be adjusted continuously to avoid drifting away from the sweet spot, a source of difficulty in experiments.

2.4 The transmon

The transmon is a modified version of the split CPB-qubit [8], which was devised to lessen the influence of $1/f$ charge noise, the principal source of dephasing in the split CPB. This is achieved by eliminating the dependence of the energy levels on gate charge. Both devices share the same effective Hamiltonian [25] but they operate at different ratios E_J/E_C: whereas it is approximately unity for the CPB, it is far greater than one for the transmon. From a technical point of view, the transmon closely resembles the split CPB qubit. The dominant feature of the transmon is an additional capacitance shunting the two Josephson junctions. An increased gate capacitance also sets it apart from its predecessor. The effective circuit diagram is shown in Fig. 2.5.

Charge dispersion

When increasing the ratio E_J/E_C, the variation of the energy levels as one sweeps the gate charge gets lesser and lesser. In fact, charge dispersion decreases exponentially with E_J/E_C. As a result, in the transmon regime, the energy levels are almost independent of the gate charge, as illustrated in 2.4. Thus, the transmon displays the desired robustness against charge noise and

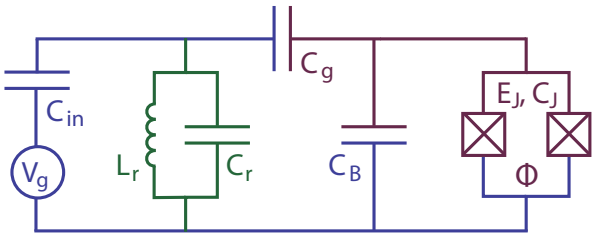

Figure 2.5: Effective circuit diagram of a transmon. The resonator (green) used for qubit control is modeled as a circuit with impedance L_r and capacitance C_r. The capacitor C_B shunts the split CPB (red). Graphic adapted from [8].

it is no longer necessary to tune the gate charge to remain at the sweet spot. In the transmon regime, the charge dispersion can be approximated by [8]

$$\epsilon_i \approx (-1)^i E_C \frac{2^{4i+5}}{i!} \sqrt{\frac{2}{\pi}} \left(\frac{E_J}{2E_C}\right)^{\frac{i}{2}+\frac{3}{4}} e^{-\sqrt{8E_J/E_C}}. \tag{2.12}$$

The expression ϵ_i is the peak-to-peak value for the charge dispersion of the ith energy level.

Anharmonicity

However, as E_J/E_C increases, the separation between the energy levels diminishes with a power law in E_J/E_C. For large enough ratios E_J/E_C the spacing of the energy levels becomes almost equidistant. Then the energy spectrum resembles the one of a harmonic oscillator. Operated in this regime, the transmon bears more resemblance to a multi-level-system than to a two-level system because of the smallness of the anharmonicity $\alpha = E_{ef} - E_{ge}$. Even though the transition matrix elements are significant only between nearest-neighbour levels, the proximity of the transition frequencies may account for some leakage in the next-to-nearest-neighbour levels during qubit operations. Therefore, care must be taken to increase E_J/E_C only so much as to keep the anharmonicity large enough for practical purposes. Since the charge dispersion decreases exponentially and the anharmonicity decreases only algebraically, this may readily be achieved.

Further properties

The theory predicts [8] that the coupling between the cavity and neighbouring transmon levels increases as E_J/E_C rises, whereas the coupling between the cavity and non-neighbouring transmon levels vanishes as E_J/E_C rises. Strong coupling between cavity and transmon allows for instance the observation of vacuum Rabi splitting, which occurs when the qubit is in resonance with the cavity. Then, the radiation transmitted through the cavity is split into two frequency lines. Strong coupling also permits a cavity coupled to two qubits to act as a photon bus, a

possible means of transporting information between distant qubits. Both effects were observed in Ref. [5].

In the dispersive regime, where the detuning between the energy-level-transitions of the transmon and the cavity are large, the transmon can be operated like the split CPB, because of the similarity of the respective Hamiltonians, cf. eqn. (2.7). The qubit-state-dependent AC-Stark effect allows us to deduce the qubit state from measurements of the transmitted amplitude and phase of a microwave probing signal sent through the cavity [8]. In practice, coherent microwave radiation $\mathcal{E}(t)$, called drive,

$$\mathcal{E}(t) = \mathcal{E}_x(t)\cos(\omega_d t + \beta) + \mathcal{E}_y(t)\sin(\omega_d t + \beta), \tag{2.13}$$

is applied to the input port of the resonator. $\mathcal{E}_x(t)$ and $\mathcal{E}_y(t)$ are the two independent quadratures of the drive and are 90°-phase shifted with respect to each other.

Experimental tests

The functionality of the transmon has been verified experimentally in many instances. An increased insensitivity to charge noise has been successfully demonstrated in Ref. [26]. The observed dephasing times go as high as roughly $T_2 = 3\,\mu\text{s}$ and the energy relaxation times reach approximately $T_1 = 1.6\,\mu\text{s}$ [25].

2.5 Pi-pulses

The π-pulses and its sibling, the $\pi/2$-pulse, are fundamental building blocks of single-qubit manipulations. Their effect can conveniently be modelled using a two-level transition exposed to radiation. Here, we consider a bound electron for simplicity. A detailed treatment can be found in Refs. [27] and [28].

Consider a quantum mechanical system described by the time-dependent Schrödinger equation

$$\mathrm{i}\hbar\frac{\partial}{\partial t}|\psi\rangle = H|\psi\rangle \tag{2.14}$$

where the Hamiltonian H is split up in two parts, $H = H_0 + H_\mathrm{i}(t)$. H_0 is the time-independent part with eigenfunctions $|\psi_i\rangle \equiv |i\rangle$ and eigenvalues $\hbar\omega_i$. $H_\mathrm{I}(t)$ is the perturbative, time-dependent part. To solve eqn. (2.14), we consider the ansatz

$$|\psi(t)\rangle = \sum_i c_i \mathrm{e}^{-\mathrm{i}\omega_i t}|\psi_i\rangle, \quad c_i \in \mathbb{C}.$$

Restricting the problem to a two-level-system, the ansatz becomes

$$|\psi(t)\rangle = c_0\mathrm{e}^{-\mathrm{i}\omega_0 t}|0\rangle + c_1\mathrm{e}^{-\mathrm{i}\omega_1 t}|1\rangle. \tag{2.15}$$

Normalisation requires that $|c_0|^2 + |c_1|^2 = 1$. If the perturbative part of the Hamiltonian is to describe radiation with constant amplitude $\mathbf{E}_0$, it is given by

$$H_I(t) = e\mathbf{r} \cdot \mathbf{E}(t), \quad \mathbf{E}(t) = \mathbf{E}_0(t) \cos \omega t,$$

where $\mathbf{r}$ is the position of the electron with respect to the nucleus. Plugging this and the ansatz (2.15) into eqn. (2.14) gives a coupled system of equations for the coefficients c_0 and c_1:

$$\begin{cases} \mathrm{i}\dot{c}_0 &= \Omega \cos \omega t \, \mathrm{e}^{-\mathrm{i}\omega_{10}t} c_1 \\ \mathrm{i}\dot{c}_1 &= \Omega^* \cos \omega t \, \mathrm{e}^{\mathrm{i}\omega_{10}t} c_0 \end{cases}, \tag{2.16}$$

where $\omega_{10} = \omega_1 - \omega_0$ is the transition frequency between states 0 and 1 and $\Omega = \mathbf{R}_{01} \cdot \mathbf{E}/\hbar$ is the so-called Rabi frequency, the product of the dipole matrix element $\mathbf{R}_{01} = e\langle 0|\mathbf{r}|1\rangle$ with $\mathbf{E}/\hbar$. The terms $\langle i|\mathbf{r}|i\rangle, i = 0, 1$ vanish because $\mathbf{r}$ is an odd operator and the states $|i\rangle$ have either even or odd parity. If we orient the electrical field vector $\mathbf{E}$ along the x-axis, $\mathbf{E}(t) = |\mathbf{E}_0| \cos \omega t \, \mathbf{e}_x$ and impose the initial conditions $c_1(t = 0) = 0$, the system (2.16) can be solved. One finds that

$$|c_1(t)|^2 = \frac{\Omega^2}{W^2} \sin^2\left(\frac{Wt}{2}\right),$$

where $W^2 \equiv \Omega^2 + (\omega - \omega_{10})^2$. So the population $|c_1(t)|^2$ of the excited state varies between 0 and a maximum of W^2/Ω^2 which is reached periodically: we observe oscillatory behaviour in response to the external field. This phenomenon is called Rabi oscillation. When the external radiation field is in resonance with the transition frequency of the two-level-system, $\omega = \omega_{10}$, $W = \Omega$ and $|c_1(t)|^2 = \sin^2(\Omega t)$. This means that the state $|1\rangle$ can be fully populated. The pulse of resonant radiation of duration $t_\pi = \pi/\Omega$,

$$\mathbf{E}(t) = \mathbf{E}_0 \chi_{[0,t_\pi]}(t) \cos \omega_{10} t,$$

is called a π-pulse. The function $\chi_{[0,t_\pi]}(t)$ is one if $t \in [0, t_\pi]$ and zero else. If the system was initially in the ground state, it results in a complete transfer of the population in the excited state:

$$|\psi(t = 0)\rangle = |0\rangle \xrightarrow{\pi\text{-pulse}} |\psi(t = t_\pi)\rangle = -\mathrm{i}|1\rangle.$$

More generally, for an arbitrary initial state, it results in

$$|\psi(t = 0)\rangle = c_0|0\rangle + c_1|1\rangle \xrightarrow{\pi\text{-pulse}} |\psi(t = t_\pi)\rangle = -\mathrm{i}(c_1|1\rangle + c_0|0\rangle).$$

A $\pi/2$-pulse lasts half the duration of a π-pulse. If the system is the ground state before the pulse, it will be mapped as follows:

$$|0\rangle \xrightarrow{\frac{\pi}{2}\text{-pulse}} \frac{|0\rangle - \mathrm{i}|1\rangle}{\sqrt{2}}.$$

That is, the excited state is mapped to an equal superposition state. Likewise, a $\pi/2$-pulse maps ground state to an equal superposition state. A note on the case where the radiation amplitude varies in time: When $\mathbf{E}_0 = \mathbf{E}_0(t)$, the Rabi frequency also varies with time, $\Omega(t) = |\mathbf{R}_{01}\mathbf{E}_0(t)/\hbar|$. The pulse area, a dimensionless quantity, is defined as

$$\Theta = \left| \frac{\mathbf{R}_{01}}{\hbar} \int_{-\infty}^{\infty} \mathrm{d}t \, \mathbf{E}_0(t) \right|.$$

If $\Theta = \pi$, the pulse is a π-pulse.

Driven qubit in the rotating frame

The Hamiltonian of the qubit exposed to coherent drive with fixed phase as in eqn. (2.13) is [29]

$$H = \frac{\hbar}{2}\omega_a\sigma_z + \hbar\Omega\Big(\cos(\omega_d t + \beta)\sigma_x + \sin(\omega_d t + \beta)\sigma_y\Big), \tag{2.17}$$

where $\hbar\Omega$ is the dipole interaction strength between the qubit and the drive and Ω is the Rabi frequency in units of angular frequency. We now transform this Hamiltonian to a frame rotating about the z-axis at the drive frequency ω_d (in angular units). This transformation is described by the unitary operator $U = e^{i\omega_d t\sigma_z/2}$. The state vector $|\psi\rangle$ is mapped to $|\tilde{\psi}\rangle = U|\psi\rangle$. From the Schrödinger equation for $|\tilde{\psi}\rangle$ one finds that the Hamiltonian H is mapped to $\tilde{H} = UHU^\dagger - i\hbar U\dot{U}^\dagger$.

If one carries out the computation in the rotating wave approximation, i.e. if one keeps only the terms oscillating at frequency ω_d and neglects those at frequency $2\omega_d$, the Hamiltonian in the new frame of reference $\tilde{H}$ becomes time-independent. It is given by

$$\tilde{H} = \frac{\hbar}{2}(\mathcal{E}_x\sigma_x + \mathcal{E}_y\sigma_y + \Delta\sigma_z). \tag{2.18}$$

where $\Delta = \omega_a - \omega_d$ is the detuning, $\mathcal{E}_x = \Omega\cos\beta$ and $\mathcal{E}_y = \Omega\sin\beta$. This Hamiltonian can compactly be written as $\tilde{H} = \frac{\hbar}{2}\mathbf{B}\cdot\boldsymbol{\sigma}$, where $B_x = \mathcal{E}_x$, $B_y = \mathcal{E}_y$ and $B_z = \Omega$. In the rotating frame, the Hamiltonian (2.17) has thus received a simple interpretation. It describes a spin 1/2 particle in an effective magnetic field $\mathbf{B}$ whose components are given by the detuning and the drives multiplied by a phase angle.

2.6 Geometric phases

In quantum mechanics, the wavefunction describing a particle acquires a phase as it evolves in time. The phase γ can be divided into a dynamic phase γ_d and a geometric phase γ_g. The dynamic phase follows from the Hamiltonian—it is the energy of the state, integrated over time and divided by the reduced Planck constant. The geometric phase, on the other hand, constitutes a 'memory' of the evolution the system has undergone [10]. If the final state $|\psi'\rangle$ is related to the initial state $|\psi\rangle$ via $|\psi'\rangle = \mathrm{e}^{\mathrm{i}\gamma}|\psi\rangle$, i.e. when the evolution is *cyclic*, $|\psi\rangle$ and$|\psi'\rangle$ lie in the same ray of the Hilbert space, since they only differ by a phase factor. If evolution is cyclic and, in addition, the evolution of the system takes places adiabatically—what in this context means slowly—, this phase is also called Berry's phase. This is a tribute to Sir M. V. Berry who first investigated it in this setting [13]. Some three decades before, S. Pancharatnam introduced geometric phases while studying the rotation of the polarisation of light [30]. A few words about the term 'geometric': the phase is geometric because it depends neither on the energy of the eigenstate nor on the rate of the evolution. It depends solely on the sequence of quantum states [10].

In the following, we show how Berry's phase arises from the Schrödinger equation with a time-dependent Hamiltonian and how it can be likened to parallel transport. Then, after a few words on generalisations and experimental tests of Berry's phase, we derive a simple expression relating it to the sequence of quantum states.

Berry's phase

Given a quantum system, described at the time $t = 0$ by a normalised wavefunction $|\psi\rangle$ in a Hilbert space $\mathcal{H}$ and a Hamiltonian H, one might want to investigate how the system evolves when H is modified from $H(0)$ to $H(T)$ during the time T. If T is large enough or the change slow enough, i.e. if H is modified adiabatically, Ehrenfest's adiabatic theorem (see, for example, Ref. [31]) implies that at $t = T$ the system will have evolved into an eigenstate of $H(T)$.

What can be said about the phase of the wavefunction in the case where $H(0) = H(T)$, implying that the evolution of the state is cyclic? The following considerations are based upon Ref. [32]. Denoting the parameters on which the Hamiltonian H depends collectively by $\mathbf{R}$, and assuming that these change adiabatically over time, $\mathbf{R} = \mathbf{R}(t)$, the Schrödinger equation describing the time evolution of $|\psi\rangle$ is

$$H(\mathbf{R}(t))|\psi(t)\rangle = \mathrm{i}\hbar\frac{\mathrm{d}}{\mathrm{d}t}|\psi(t)\rangle. \tag{2.19}$$

If the state at $t = 0$ is in the nth normalised eigenstate, $|\psi(0)\rangle = |n, \mathbf{R}(0)\rangle$, where

$$H(\mathbf{R}(0))|n, \mathbf{R}(0)\rangle = E_n(\mathbf{R}(0))|n, \mathbf{R}(0)\rangle,$$

what is the state at some $t > 0$? At a glance, one is tempted to propose

$$|\psi(t)\rangle = \exp\left\{-\frac{\mathrm{i}}{\hbar}\int_0^t \mathrm{d}t'\, E_n(\mathbf{R}(t'))\right\}|n, \mathbf{R}(t)\rangle \equiv \mathrm{e}^{\mathrm{i}\gamma_\mathrm{d}},$$

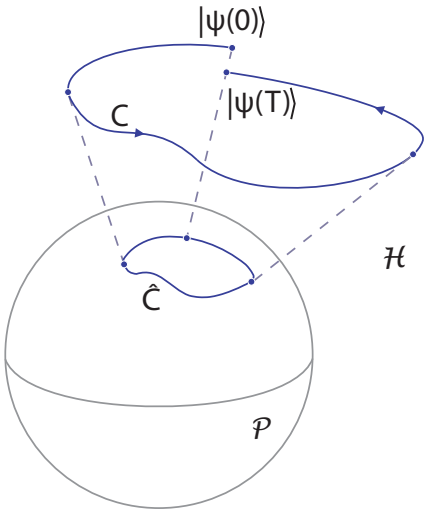

Figure 2.6: If the evolution of the Hamiltonian is adiabatic and cyclic, the state vector $|\psi(T)\rangle$ after the evolution will lay in the same ray as the state $|\psi(0)\rangle$ before the evolution. However, the phase may differ. This also appears in the properties of the curves C and $\hat{C}$, describing the curve traced out by $|\psi(t)\rangle$ in the Hilbert space $\mathcal{H}$ and in the projective Hilbert space $\mathcal{P}$, respectively: whereas C is open, making the phase difference manifest, the curve $\hat{C}$ is closed.

that is, the initial state multiplied by a dynamical phase factor. The dynamical phase is

$$\gamma_{\mathrm{d}} = -\frac{1}{\hbar}\int_0^t \mathrm{d}t' E_n(\mathbf{R}(t')).$$

However, this ansatz does not satisfy the Schrödinger equation (2.19). One therefore makes the following educated guess,

$$|\psi(t)\rangle = \exp\left\{\mathrm{i}\gamma_{\mathrm{g}}(t) - \mathrm{i}\int_0^t \mathrm{d}t'\, E_n(\mathbf{R}(t'))\right\}|n,\mathbf{R}(t)\rangle,$$

where $\gamma_{\mathrm{g}}(t)$ is an extra phase, the geometrical phase. Plugging this into the Schrödinger equation, one finds

$$H(\mathbf{R}(t))|\psi(t)\rangle = E_n(\mathbf{R}(t))|\psi(t)\rangle$$

for the left-hand side and

$$\mathrm{i}\hbar\frac{\mathrm{d}}{\mathrm{d}t}|\psi(t)\rangle = \Big(-\hbar\dot{\gamma}_{\mathrm{d}}(t) + E_n(\mathbf{R}(t))\Big)|\psi(t)\rangle + \exp\left\{\mathrm{i}\gamma_{\mathrm{g}}(t) - \frac{\mathrm{i}}{\hbar}\int_0^t \mathrm{d}t'\, E_n(\mathbf{R}(t'))\right\}\mathrm{i}\hbar\frac{\mathrm{d}}{\mathrm{d}t}|n,\mathbf{R}(t)\rangle$$

for the right-hand side. Equating both sides and multiplying the equation by $\langle\psi(t)|$ gives

$$\dot{\gamma}_{\mathrm{g}}(t) = \langle n,\mathbf{R}(t)|\mathrm{i}\frac{\mathrm{d}}{\mathrm{d}t}|n,\mathbf{R}(t)\rangle,$$

which can be integrated to

$$\gamma_{\mathrm{g}}(t) = \mathrm{i}\int_0^t \mathrm{d}t' \,\langle n, \mathbf{R}(t')|\frac{\mathrm{d}}{\mathrm{d}t'}|n, \mathbf{R}(t')\rangle = \mathrm{i}\int_{\mathbf{R}(0)}^{\mathbf{R}(t)} \mathrm{d}\mathbf{R}\,\langle n, \mathbf{R}|\nabla_{\mathbf{R}}|n, \mathbf{R}\rangle. \tag{2.20}$$

The phase $\gamma_{\mathrm{g}}(t)$ should be real to preserve the norm-squared of the wavefunction. This is the case, since

$$\begin{aligned}\Im\{\gamma_{\mathrm{g}}(t)\} &= \Im\left\{\mathrm{i}\langle n, \mathbf{R}(t)|\frac{\mathrm{d}}{\mathrm{d}t}|n, \mathbf{R}(t)\rangle\right\} \\ &= \frac{1}{2}\left(\langle n, \mathbf{R}(t)|\frac{\mathrm{d}}{\mathrm{d}t}|n, \mathbf{R}(t)\rangle + \text{c.c.}\right) \\ &= \frac{1}{2}\frac{\mathrm{d}}{\mathrm{d}t}\langle n, \mathbf{R}(t)|n, \mathbf{R}(t)\rangle = 0\end{aligned}$$

due to the normalisation of the state. If the evolution is cyclic, the geometrical phase change is

$$\gamma_{\mathrm{g}} = \mathrm{i}\int_{\mathbf{R}(0)}^{\mathbf{R}(T)} \mathrm{d}\mathbf{R}\,\langle n, \mathbf{R}(t)|\nabla_{\mathbf{R}}|n, \mathbf{R}(t)\rangle.$$

This quantity does not necessarily vanish, since the integrand may not be a total derivative. However, it is independent of the rate at which the path $\mathbf{R}([0, T])$ is traversed. In the above case, where both adiabaticity and cyclicity are assumed, the geometrical phase is called Berry's phase.

Connection to Parallel transport

The aim of this paragraph is to elucidate the connection [10] between classical parallel transport and Berry's phase. Parallel transport of a vector along a curve in a plane merely amounts to moving the vector along the curve while keeping its length and direction constant. Parallel transport along a curve on a curved surface is slightly more intricate. One requires the following: that (a) the length of the vector and (b) the angle between the vector and the surface normal should be kept constant. The special case of the transformation undergone by a vector parallel transported along a closed curve P is called a holonomy transformation. If the closed curve lies in a plane, the transported vector is identical to the initial vector. If, however, the closed curve lies on a sphere with radius r, the vector is rotated by an angle α which is equal to the solid angle subtended by the curve, i.e. $\alpha = A/r^2$, where A is the area on the sphere enclosed by the closed curve. To illustrate this property, consider a vector $\mathbf{v}_i$ which is initially at the north pole of the sphere and points along a meridian, as depicted in Fig. 2.7. Parallel-transport it along this meridian until it reaches the equator, then let it move along a quarter of the equator. Finally, parallel-transport it along the new meridian until it reaches the north pole again. The parallel-transported vector $\mathbf{v}_f$ differs from $\mathbf{v}_i$: since the area enclosed by the curve P is one eighth of the surface of the sphere, $A = 4\pi r^2/8 = \frac{1}{2}\pi r^2$, $\mathbf{v}_i$ has been rotated by an angle $\alpha = \frac{1}{2}\pi r^2/r^2 = \pi/2$.

How can classical parallel transport help us gain an understanding of Berry's phase? Consider a spin vector $\mathbf{S}$ in a magnetic field $\mathbf{B}$, with $\mathbf{S}$ being parallel to $\mathbf{B}$. Then, vary the direction of

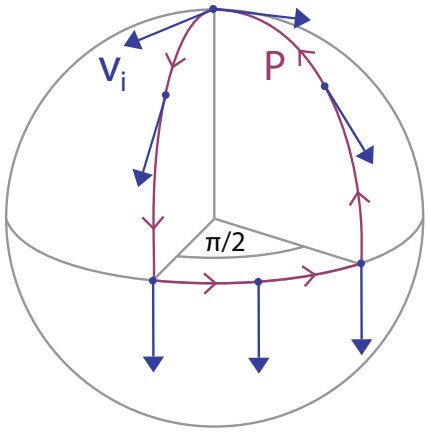

Figure 2.7: Illustration of parallel transport on a sphere. The vector $\mathbf{v}_i$ is transported along a meridian, along the equator and finally along a new meridian. It ends up rotated when it reaches its original position. Figure adapted from [29].

B adiabatically, so that the **S** follows **B** when **B** traces out a curve C on a sphere with radius $S = |\mathbf{S}|$. Let us consider what happens to a vector parallel-transported along C. Imagine a cartesian triad transported along C, with its z-axis pointing radially, and the (x, y)-plane being parallel-transported. If C is closed, any vector which keeps a fixed orientation with respect to this triad will reach its departure point rotated about the z-axis by the angle α. So the spin vector S will be rotated, too, and this changes the phase of the spin wavefunction by $\gamma_g = -\alpha/2$, the geometric phase. In addition, because the spin exposed to a magnetic field undergoes Larmor precession with frequency ω_L about the axis $\boldsymbol{\omega}_L$, the spin wavefunction also accumulates a dynamical phase γ_d.

Generalisations of Berry's phase

In the above paragraph, two assumptions were made: first, that **B** should be modified adiabatically and second, that **S** should be parallel (or antiparallel) to **B**. However, as Aharonov and Anandan demonstrated [33], both assumptions are not necessary. As long as **B** is varied in such a way that **S** follows the same path C, the geometric phase γ_g will be the same, the motion need not be adiabatic. As for the angle δ between **S** and **B**, it determines how much dynamical phase the qubit acquires. The angular frequency of precession of the qubit around the spin axis **S** is the projection of the angular momentum vector ω_L onto **S**. Therefore, this angular frequency is $\omega_L \cos\delta$. The case where **S** is parallel to **B** implies $\delta = 0$, and the angular frequency of precession is, as above, $\omega_L \cos(0) = \omega_L$.

Berry's phase appears in still a more general context. Samuel and Bhandari [34] proved that the evolution of the quantum system need not be cyclic, i.e. the final state need not lay in the same ray as the initial state. Then, the curve C traced out on the sphere is no longer closed. Berry's phase appears as an integral over the surface (the ray space) bounded by the contour

C closed by any geodesic curve joining the initial and final state. The geodesics of the ray space are defined via the metric on the ray space, which is induced by the inner product on the Hilbert space. Furthermore, Samuel and Bhandari showed that the evolution of the quantum system may be interrupted by quantum measurements. Both generalisations, Aharanov and Anandan's, as well as Samuel and Bhandari's, are based on the work by Pancharatnam.

The geometric phase has also been extended to the case involving more than one state, giving rise to so-called off-diagonal geometric phases [35]. The analysis of the Berry phase in terms of differential geometry has been carried out by Simon [36].

Experimental tests

Berry's phase has been observed in a variety of settings. Among the first observations are, in 1986, the detection using photons in optical fibre [37] and in 1987, the observation using spin-polarised neutrons [38] and the detection using the spins of chlorine nuclei within a crystal of sodium chlorate [39]. The nonadiabatic but cyclic phase was observed in the same year in a system of coupled protons [40]. The noncyclic phase was measured in a spin-polarised neutron experiment [41]. The first observation of Berry's phase in a solid-state qubit took place in Prof. Wallraff's research group in 2007 [29]. In 2008, Berry's phase was first determined in a superconducting charge pump [42].

Derivation of Berry's phase

The following is a derivation of Berry's phase, closely following Berry's original paper [13]. We find a simple expression for the phase based on the sequence of quantum states the system has followed.

Working in a three dimensional parameter space, the geometrical phase as defined in (2.20) can be rewritten by means of Stoke's theorem as

$$\gamma_g = \gamma_g(n, C) = -\Im \int_C \mathrm{d}\mathbf{S} \cdot \mathrm{rot}\langle n, \mathbf{R})|\nabla_{\mathbf{R}}|n, \mathbf{R}(t)\rangle,$$

where C is the closed contour traced out by $\mathbf{R}(t)$. Writing $|n, \mathbf{R}(t)\rangle \equiv |n\rangle$ and $\frac{\partial}{\partial j} \equiv \partial_j$ for simplicity and using that

$$\Big(\mathrm{rot}\langle n|\nabla|n)\rangle\Big)_i = \varepsilon_{ijk}\Big(\langle\partial_j n|\partial_k n\rangle + \langle n|\partial_j\partial_k n\rangle\Big) = \varepsilon_{ijk}\Big(\langle\partial_j n|\partial_k n\rangle\Big) = \Big(\nabla_n \wedge \nabla n\Big)_{i'}$$

one finds

$$\gamma_g(n, C) = -\Im \int_C \mathrm{d}\mathbf{S} \cdot \langle\nabla n| \wedge |\nabla n\rangle = -\int_C \mathrm{d}\mathbf{S} \cdot \Im \sum_{\substack{m \\ m\neq n}} \langle\nabla n|m\rangle \wedge \langle m|\nabla n\rangle \equiv -\int_C \mathrm{d}\mathbf{S} \cdot \mathbf{V}_n(R). \quad (2.21)$$

In the last step,

$$(\nabla n \wedge \nabla n)_i = \varepsilon_{ijk}\left(\langle\partial_j n| \sum_m |m\rangle\langle m||\partial_k n\rangle\right) = \varepsilon_{ijk}\left(\sum_{\substack{m \\ m\neq n}} \langle\partial_j n|m\rangle\langle m|\partial_k n\rangle + \langle\partial_j n|n\rangle\langle n|\partial_k n\rangle\right)$$

was used. The last term of the above expression vanishes in (2.21) because $\langle n|\partial_k n\rangle$ is purely imaginary. From the Schrödinger equation (2.19), one has

$$\begin{aligned} & \nabla H(\mathbf{R})|n\rangle + H|\nabla n\rangle = \nabla E_n(\mathbf{R})|n\rangle + E_n|\nabla n\rangle \\ \Longleftrightarrow \quad & \langle m|\nabla H(\mathbf{R})|n\rangle + \langle m|H|\nabla n\rangle = (\nabla E_n(\mathbf{R}))\langle m|n\rangle + E_n\langle m|\nabla n\rangle \\ \Longleftrightarrow \quad & \langle m|\nabla n\rangle = \frac{\langle m|\nabla H(\mathbf{R})|n\rangle}{E_n - E_m}, \end{aligned}$$

as long as $m \neq n$. Inserting this into (2.21) gives the following result:

$$\gamma_{\mathrm{g}} = -\int_C \mathrm{d}\mathbf{S} \cdot \Im \sum_{\substack{m \\ m\neq n}} \frac{\langle n(\mathbf{R})|\nabla_{\mathbf{R}} H(\mathbf{R})|m(\mathbf{R})\rangle \times \langle m(\mathbf{R})|\nabla_{\mathbf{R}} H(\mathbf{R})|n(\mathbf{R})\rangle}{(E_m - E_n)^2}.$$

Here, a comment is in order. Because the geometric phase is now explicitly independent of $|\nabla n\rangle$, any solutions of the Schrödinger equation may be used to compute it without affecting its value. Is it gauge invariant because it is independent of the phase of $|n\rangle$. This is remarkable because, as can be seen from (2.21), γ_{g} depends on $\langle n|\nabla n\rangle$. And the expression $\langle n|\nabla n\rangle$ *does* depend on the choice of phase: if $|n\rangle \mapsto \mathrm{e}^{\mathrm{i}\mu(\mathbf{R})}|n\rangle$, then $\langle n|\nabla n\rangle \mapsto \langle n|\nabla n\rangle + \mathrm{i}\nabla\mu$.

What can be said about the geometric phase if there is a degeneracy in parameter space? As can be seen from eqn. (2.21), the geometric phase is dominated by the states involved in the degeneracy if C lies close to it. We consider the twofold degeneracy of the energy levels of a spin 1/2 system in the absence of a magnetic field. This situation corresponds to a degeneracy point $\mathbf{R}^*$ in parameter space. As soon as the magnetic field is non-zero, the degeneracy is lifted, i.e. one moves away from $\mathbf{R}^*$ to a point $\mathbf{R}$ in its the neighbourhood. We denote the two states involved in the degeneracy + and −, with $E_+(\mathbf{R}) \geq E_-(\mathbf{R})$. Then, expanding the Hamiltonian around $\mathbf{R}^*$, $\nabla_{\mathbf{R}} H(\mathbf{R}) \approx \nabla_{\mathbf{R}} H(\mathbf{R}^*)$, one has

$$\begin{aligned} \mathbf{V}_+(\mathbf{R}) &= \Im \sum_{\substack{m \\ m\neq +}} \frac{\langle +(\mathbf{R})|\nabla_{\mathbf{R}} H(\mathbf{R})|m(\mathbf{R})\rangle \times \langle m(\mathbf{R})|\nabla_{\mathbf{R}} H(\mathbf{R})| + (\mathbf{R})\rangle}{(E_m - E_+)^2} && (2.22) \\ &= \Im \sum_{\substack{m \\ m\neq +}} \frac{\langle +(\mathbf{R})|\nabla_{\mathbf{R}} H(\mathbf{R}^*)|m(\mathbf{R})\rangle \times \langle m(\mathbf{R})|\nabla_{\mathbf{R}} H(\mathbf{R}^*)| + (\mathbf{R})\rangle}{(E_m - E_+)^2} && (2.23) \\ &\approx \Im \frac{\langle +(\mathbf{R})|\nabla_{\mathbf{R}} H(\mathbf{R}^*)| - (\mathbf{R})\rangle \times \langle -(\mathbf{R})|\nabla_{\mathbf{R}} H(\mathbf{R}^*)| + (\mathbf{R})\rangle}{(E_+ - E_-)^2}. && (2.24) \end{aligned}$$

Because only the energy states involved in the degeneracy make sizeable contributions to the sum, the other terms of the sum may be dropped.

We now take, without loss of generality, $E_\pm(\mathbf{R}^*) = 0$ and $H(\mathbf{R}) = 0$. The most general Hamiltonian coupling two states is of the form

$$H(\mathbf{R}) = \frac{1}{2}\begin{pmatrix} Z & X - \mathrm{i}Y \\ X + \mathrm{i}Y & Z \end{pmatrix}.$$

Its eigenvalues are $E_+(\mathbf{R}) = \frac{1}{2}\sqrt{X^2 + Y^2 + Z^2} \equiv \frac{1}{2}R$ and $E_-(\mathbf{R}) = -\frac{1}{2}R$. It has the additional property that $\nabla H = \frac{1}{2}\boldsymbol{\sigma}$. The computation of the geometric phase is greatly simplified by

exploiting the isotropy of the spin. We rotate the coordinate system so that $\mathbf{R}$ is parallel to the $Z-$axis, $\mathbf{R} = (0, 0, Z)$. Then, using

$$\sigma_x|+\rangle = \begin{pmatrix} 0 & 1 \\ 1 & 0 \end{pmatrix}\begin{pmatrix} 1 \\ 0 \end{pmatrix} = \begin{pmatrix} 0 \\ 1 \end{pmatrix} = |-\rangle, \quad \sigma_x|-\rangle = |+\rangle$$

and the similar relations $\sigma_y|\pm\rangle = \pm\mathrm{i}|\mp\rangle, \sigma_z|\pm\rangle = \pm|\pm\rangle$, one has

$$\begin{aligned}(\mathbf{V}_+)_x &= \Im\Big\{\langle+|\frac{\boldsymbol{\sigma}}{2}|-\rangle \times \langle-|\frac{\boldsymbol{\sigma}}{2}|+\rangle(E_+ - E_-)^2\Big\}_x \\ &= \frac{1}{4R^2}\Im\Big\{\langle+|\sigma_y|-\rangle\langle-|\sigma_z|+\rangle - \langle+|\sigma_z|-\rangle\langle-|\sigma_y|+\rangle\Big\} \\ &= \frac{1}{4R^2}\Im\Big\{\langle+|(-\mathrm{i})|+\rangle\langle-|1|+\rangle - \langle+|(-1)|-\rangle\langle-|\mathrm{i}|+\rangle\Big\} = 0\end{aligned}$$

and, similarly, $(\mathbf{V}_+)_y = 0$ as well as $(\mathbf{V}_+)_z = \frac{1}{4R^2}\Im\{\mathrm{i} - (-\mathrm{i})\} = \frac{1}{2R^2}$. Consequently, when one rotates back the axes, the result is $\mathbf{V}_+ = \frac{1}{2R^2}\cdot\frac{\mathbf{R}}{R}$. Finally, from (2.21), we find that the geometric phase is

$$\gamma_{\mathrm{g}}(+, C) = -\frac{1}{2}\int_C \mathrm{d}\mathbf{S}\cdot\frac{\mathbf{R}}{R^3} \equiv -\frac{1}{2}\alpha(C), \tag{2.25}$$

where $\alpha(C)$ is the solid angle subtended by the curve C at the degeneracy point $\mathbf{R}^*$. Now, since $\mathbf{V}_+ = -\mathbf{V}_-$, cf. eqn. (2.22), $\gamma_{\mathrm{g}}(-, C) = +\frac{1}{2}\alpha(C)$. In brief, the geometrical phase factor associated with C is

$$\mathrm{e}^{\mathrm{i}\gamma_{\mathrm{g}}(\pm,C)} = \mathrm{e}^{\mp\frac{1}{2}\mathrm{i}\alpha(C)}.$$

This is the central result of this section: the geometric phase is, up to a sign, half the solid angle $\alpha(C)$ of the curve C in parameter space.

3 Experimental techniques and equipment

This chapter is devoted to an overview of the techniques and equipment used in this thesis. After a description of the artificial atom and its immediate environment, the sample, we move on to the dilution refrigerator. A few paragraphs on signal processing, the qubit-readout mechanism and qubit spectroscopy conclude this chapter.

3.1 The sample

In the following, we describe the physical implementation of the microwave cavity QED setup used in this experiment. In essence, it consists of a resonator coupled to a transmon qubit mounted on a chip ('on chip' cavity QED).

The resonator

The resonator is formed by a one-dimensional transmission-line resonator, consisting of a section of a superconducting coplanar waveguide (CPW). The advantage of the architecture combining a one-dimensional resonator and a CPB is the strong coupling, 10^4 times stronger than what is achievable in atomic systems such as 3D microwave cavities and Rydberg atoms. This is possible because the mode volume of the 1D resonator is small compared to the mode volume of a three-dimensional cavity of similar wavelength, and because of the large geometric capacitance of the CPB [43].

Specifically, CPWs can be designed to operate at frequencies of 10 GHz, allowing to use the qubit in a broad frequency range. The frequency of the cavity depends on the geometry of the resonator. Accurate manufacturing of CPW resonators with designed coupling has been demonstrated in Ref. [44]. Apart from the technical ability per se, this is of relevance since different experiments demand different quality factors. For instance, fast measurements on the qubit require low-Q resonators, while storage of photons requires high-Q resonators.

A CPW consists of two semi-infinite ground planes mounted on a dielectric substrate separated by a slot. In the centre of this slot lies the centre strip conductor [45]. A schematic representation in shown is Fig. 3.1. The theoretical description of the resonator relies on transmission line theory (as opposed to circuit theory) because of the electrical size of the circuit: circuit theory is applicable only if the wavelength of the radiation by far exceeds the dimensions of the circuit. But here, the wavelength of the microwave radiation in the cavity is comparable to the length of the transmission line. The CPW can nevertheless be modelled using circuit theory by using the equivalent lumped circuit representation: an infinitesimal piece of the transmission line is

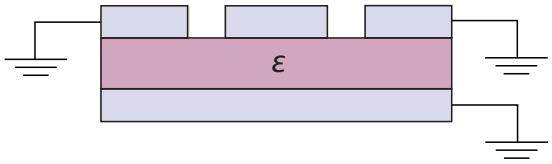

Figure 3.1: Schematic of the section of a CPW. Conducting materials are shown in blue, dielectric materials in red. The dielectric material with permittivity ε is mounted on top of a conducting ground plane (bottom). On top the dielectric plane there are two ground planes, to the left and to the right. Between these ground planes, separated by slots (white) lies the centre strip conductor.

described as a circuit having a series inductance per unit length and a shunt capacitance per unit length. (For further details see [46], chapter 2.1). The lumped circuit representation is convenient for developing an intuitive understanding of the resonator and, what is more, for the quantisation of the resonator.

The resonator is made of niobium and is fabricated using optical lithography. Because niobium is superconducting in liquid helium, the resonator can be tested conveniently. The resonator couples to the input and output transmission lines via gap capacitors. (For increased coupling capacitances, finger capacitors may be used.) These capacitors can be likened to the mirrors found at either end of an optical Fabry-Pérot cavity. Their capacitances determine the quality factor of the cavity. The resonator rests on a sapphire substrate, a material chosen for its low dielectric losses.

The transmon qubit

The sample contains two transmons placed in the cavity at an antinode of the standing wave forming in the cavity. The transmons are made of aluminium. Aluminium oxide serves as tunnel barrier in the Josephson junction. The transmons were manufactured using electron beam lithography. Each transmon can be probed by two channels: either the signal reaches the transmon via the resonator, or it is applied directly through a gate line capacitively coupled to the transmon. An optical microscope image of the sample is shown in Fig. 3.2. With the gate lines, it is possible to address each qubit locally, suppressing coupling to the other qubit. Experiments using sideband transitions to generate entanglement between a qubit and the resonator (or between two qubits) made use of the gatelines [47]. However, the gatelines were not used in the measurements presented here.

The sample is mounted onto a sampleholder and grounded using wire-bonds. The solenoids used to tune the energy levels of the qubits are attached to the sampleholder as well and produce a homogeneous magnetic field that extends over the SQUID loops.

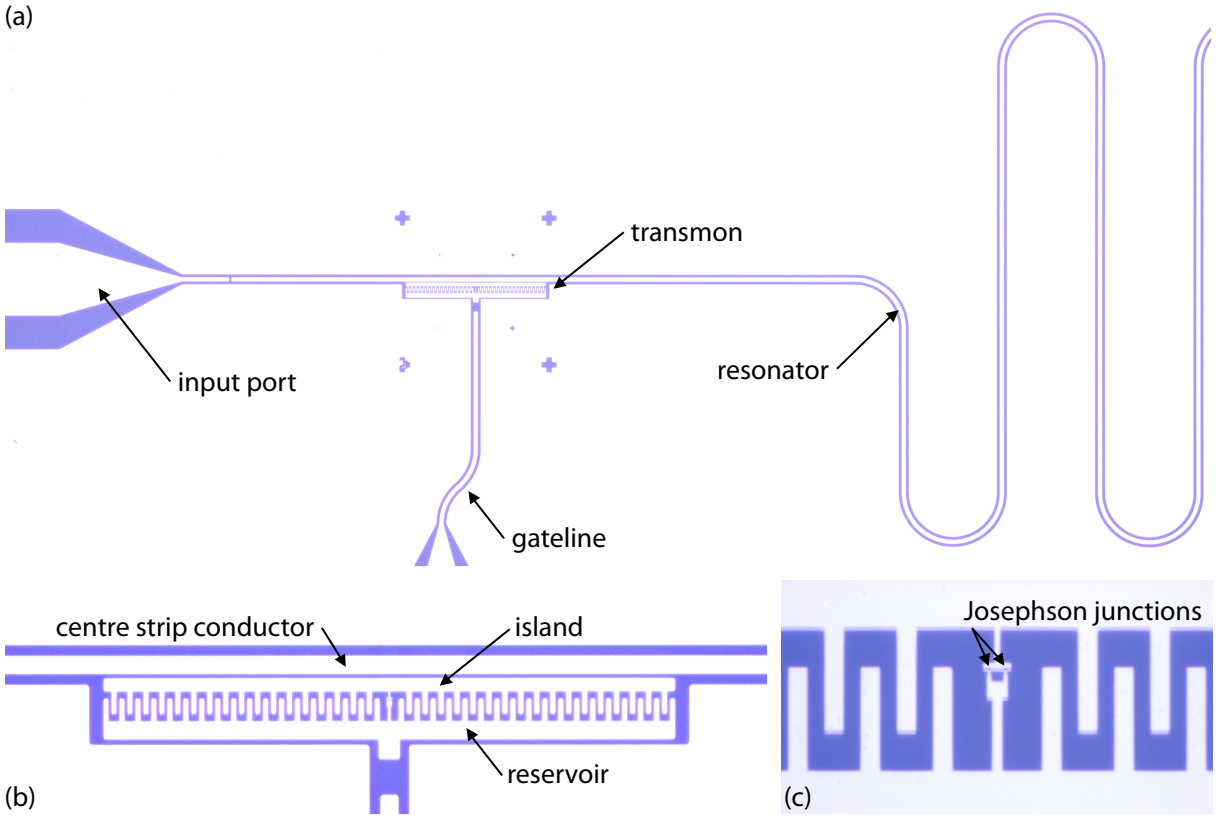

Figure 3.2: False-colour rendering of an optical microscope images of the sample. Superconducting materials (Nb, Al) are shown in white, whereas dielectric materials are blue. **(a)** A detail of the on-chip cavity QED system: a transmon inserted in the resonator, capacitively coupled to the gateline and the input port. The meanders of resonator do not detract from its functionality as long as the curvature radius is far smaller than the transverse dimensions. On the left, the narrowing of the input port of the resonator is visible. The input and output port being larger than the centre slot, their size is continuously reduced at either connection point to make sure they are impedance-matched with the external lines at every point. **(b)** The transmon qubit (300 µm across) embedded in the strip line. The dielectric element (blue) that separates the centre strip conductor from the CPB-island couples them capacitively. The reservoir is also capacitively coupled to the bottom ground plane (bottom, white). As in a split-CPB, the island and the reservoir are connected by two Josephson junctions in the centre of the finger-capacitor (meandering blue line). The finger-capacitor shunting the island and the reservoir is specific to the transmon. **(c)** Detail of the centre of the transmon. The two Josephson junctions (200 nm × 200 nm) are apparent as small structures. The sample was fabricated and imaged by Johannes Fink.

3.2 The dilution refrigerator

The sample is placed into a dilution refrigerator and kept at a temperature of about 20 mK, where both the niobium and the aluminium are superconducting. At a temperature this low, thermal excitations of the transmon become negligible and the model described in section 2.2 is accurate. It is not clear whether there is quasiparticle excitations in the the transmon. However, because they are of no importance at temperatures below ≈ 20 mK, the number of excess Cooper pairs with respect to a neutral background may be identified with the charge Q of the CPB [3].

3.3 The measurement technique

In the dispersive regime, where the resonant coupling between the single mode of the electromagnetic field in the cavity to the two level system is small compared to the atom-cavity detuning, the readout of the qubit is performed by probing the resonator. The cavity is irradiated with microwave radiation and the state of the qubit is encoded in the transmitted microwave radiation.

Signal processing

The signals are produced using an arbitrary waveform generator (AWG) and microwave generators. They are sent into the fridge at powers ranging from -50 dBm to 20 dBm. A series of attenuators and filters reduce the signals to a power of some attowatts and filter out noise before they reach the sample. The signals transmitted through the resonator are amplified again, filtered and finally analysed. Because the transmitted signal is at frequencies in the range of some GHz, it needs to be downconverted in frequency by about three orders of magnitude before the computerised data acquisition takes place. This is achieved by using an IQ-mixer as analogue downconverter. The transmitted signal, RF, with frequency ω_{RF} is split into two parts of equal amplitude. The input from the so-called local oscillator, LO, typically of frequency $\omega_{\text{LO}} = \omega_{\text{RF}} - 10\,\text{MHz}$, is also split into two parts of equal amplitude, and one of the signals is phase-shifted by 90°. These four signals are now mixed two by two, producing the outputs I and Q, the so-called I quadrature and Q quadrature. Both I and Q are a superposition of two waves oscillating at frequencies $\omega_{\text{RF}} + \omega_{\text{LO}}$ and $\omega_{\text{LO}} - \omega_{\text{RF}}$, respectively. A low pass filter then eliminates the fast oscillating components in both quadratures. The full information of the RF signal is finally recovered: the amplitude is $\sqrt{I^2 + Q^2}$ and the phase is $\arg(I + \mathrm{i}Q)$.

A detailed description of signal processing and a deep account on data acquisition can be found in Ref. [48].

Dispersive readout and population reconstruction

The properties of dispersive readout are extensively discussed in Ref. [49]. Here, a synopsis is deemed sufficient. In the dispersive regime, the qubit-resonator system can be modeled by the

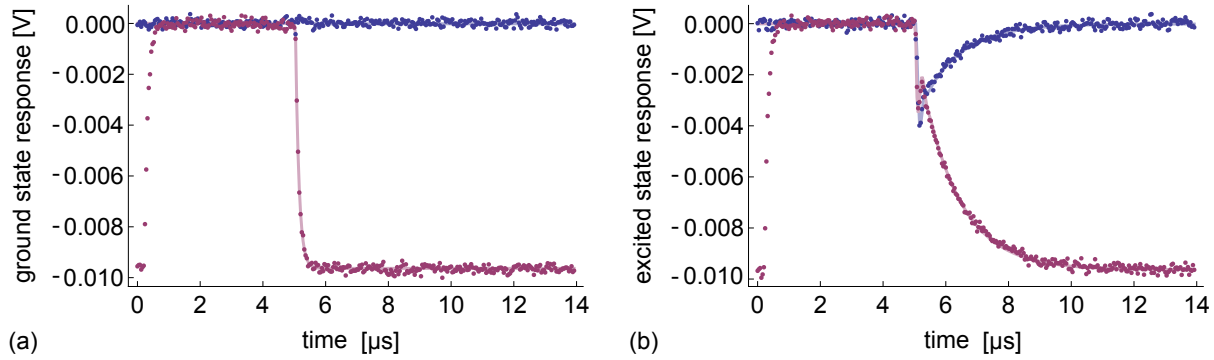

Figure 3.3: The I-quadrature (blue points) and Q-quadrature (magenta points) of the transmitted signal probing the qubit state. The lines are the theoretical responses numerically computed by fitting the cavity Bloch equations to the collected data. **(a)** Ground state response. **(b)** Excited state response. In both (a) and (b), the measurement pulse is switched on after 5 μs and the responses reach a steady state after ≈ 12 μs.

dispersive Jaynes-Cummings Hamiltonian (2.7). The RF field used to manipulate the qubit gives an additional contribution to the Hamiltonian. Incorporating dephasing and dissipation, the dynamics of the system are encapsulated in a Lindblad-type master equation. This first-order differential equation leads to a complete set of eight coupled differential equations of motion for the Bloch vector $\langle\sigma\rangle$, the resonator field operators $\langle a\rangle$, $\langle a^\dagger a\rangle$ and $\langle a\sigma\rangle$. These equations are known as the Cavity-Bloch equations and can be solved numerically.

The qubit state is probed with so-called (strong) pulsed measurements. In contrast to (weak) continuous measurements, the measurement signal is applied only after completion of the qubit state preparation, thus avoiding measurement-induced dephasing and undesirable shifts of the qubit transition frequency due to photons populating the resonator (AC-Stark shift [22]). In this context, weak and strong refer to the number of intra-cavity photons. From the point of view of quantum mechanics, both types of measurement are weak measurements, in the sense that the coupling between measured system and measuring device is weak.

When probing the resonator at its resonance frequency, the resonator response depends on the state of the qubit, cf. Fig. 3.3. If the qubit is prepared in the ground state $|g\rangle$, the Q quadrature reaches the steady state exponentially with a rate given by the photon decay rate κ, whereas the I quadrature remains zero. If, on the other hand, the qubit is in the excited state $|e\rangle$ before the measurement, both quadratures are non-vanishing. The lifetime T_1 of the excited state is extracted from the fit of these quadratures to the Cavity-Bloch equations. For a general qubit superposition state $|\psi\rangle$, the population is reconstructed from the area enclosed between the response of $|\psi\rangle$ and the ground-state response. This area is proportional to the excited state population.

Performing spectroscopy

Qubit spectroscopy, that is, determining the transition frequency between the different levels of the transmon, is performed by irradiating the system with two signals. In addition to the RF-signal described above, a spectroscopy signal is sent into the cavity. When the spectroscopy signal is in resonance with a transmon transition frequency, the transmitted RF-amplitude drops due to the shift of the resonance frequency. This dip in amplitude has the shape of a lorentzian line whose width is inversely proportional to the power of the spectroscopy signal and the lifetime of the qubit. It occurs because the resonant spectroscopy tone induces incoherent Rabi oscillations in the qubit.

4 Experiments

4.1 Characterisation of the qubit

The qubit has a maximum Josephson energy of $E_{\mathrm{J,max}} = 31.37\,\mathrm{GHz}$ and a Coulomb energy $E_{\mathrm{C}} = 0.320\,\mathrm{GHz}$, the ratio is approximately $E_{\mathrm{J,max}}/E_{\mathrm{C}} = 98$. The energy relaxation time T_1 inferred from population reconstruction varies rather much in time when measured at the same qubit transition frequency. It often lies in the range of $1.0\,\mu\mathrm{s}$ and $1.2\,\mu\mathrm{s}$. The coupling strength between qubit and resonator is $g/2\pi = 115\,\mathrm{MHz}$. The qubit transition frequencies used for the measurement of geometric phases are $\omega_{ge} = 5.541\,\mathrm{GHz}$ and $\omega_{ef} = 5.198\,\mathrm{GHz}$, implying a qubit anharmonicity of $\alpha = 343\,\mathrm{MHz}$. At these transition frequencies, $E_{\mathrm{J}} = 13.42\,\mathrm{GHz}$ and therefore $E_{\mathrm{J}}/E_{\mathrm{C}} = 42$, setting the qubit into the transmon regime.

4.2 Description of microwave drive pulses

As described in section 2.4, the ratio $E_{\mathrm{J}}/E_{\mathrm{C}}$ determines at the same time the remaining charge dispersion and the degree of anharmonicity. In our sample $E_{\mathrm{J}}/E_{\mathrm{C}}$ is large and therefore the anharmonicity is small. This means that with conventional square or gaussian pulses some coupling to leakage levels cannot be avoided, this is especially true for small pulse lengths. Since increasing the pulse length is ultimately undesirable—the gate operation time should be as short as possible to keep decoherence effects under control—, a different solution must be found. Motzoi et al. [50] proposed an analytical approach called derivative removal by adiabatic gate, or DRAG, in order to prevent population leakage.

DRAG pulses

A common way of countering leakage into the third level is not to use pulses with a square envelope, but rather pulses with a Gaussian or a tangential envelope. A Fourier analysis of these envelopes shows that they give rise to less leakage. DRAG pulses are an adaptation of Gaussian pulses, derived in a model where the multilevel-system is approximated by a three-level system whose two lowest levels represent the qubit and excitation of the third level represents leakage.

Using the second quadrature.— The qubit is, as usual, manipulated by means of monochromatic microwave pulses with two quadratures $\mathcal{E}_x(t)$ and $\mathcal{E}_y(t)$ of frequency ω_d. We assume that the pulse is applied on the $\mathcal{E}_x(t)$-quadrature. Then, by transforming the effective Hamiltonian of the three-level-system into the qubit subspace, it becomes apparent [50] that leakage can be cancelled to order $\mathcal{E}_x^4/\alpha^3$ by simultaneously (a) sending a pulse on the second quadrature $\mathcal{E}_y(t)$

and (b) adjusting the detuning $\Delta = \omega_{ge} - \omega_d$. Here, α is the anharmonicity as introduced in section 2.4.

As far as the second quadrature is concerned, it needs to be set to $\mathcal{E}_y(t) = -\dot{\mathcal{E}}_x(t)/\alpha$. That is, leakage can be prevented by applying a 90°-phase shifted pulse proportional to the time derivative of the desired pulse. This is implemented in our version of the DRAG pulse.

Ramping the phase.— The detuning, on the other hand, needs to be adjusted to $\Delta = (\lambda^2 - 4)\mathcal{E}_x(t)^2/4\alpha$, where λ is the ratio of the strength of the $|e\rangle \to |f\rangle$-transition to the strength of the $|g\rangle \to |e\rangle$-transition (in terms of dipole matrix elements). In other words, a detuning growing quadratically in the amplitude $\mathcal{E}_x(t)$ of the carrier is able to compensate leakage. This feature was added to our DRAG pulses, resulting in DRAG pulses with phase ramping.

Both pulse types are based on truncated gaussian pulses. Their envelope is the central portion of a Gaussian with standard deviation σ, truncated symmetrically at a time σt around the centre of the Gaussian. The truncation parameter t determines the flatness of the extracted portion of the Gaussian. Truncation is necessary to end the pulses at zero amplitude.

The pulse with variable phase has two scale parameters. Consider the case where we want to apply a pulse on the $\mathcal{E}_x(t)$-quadrature. Then, as described above, a compensation pulse is applied on the second quadrature $\mathcal{E}_y(t)$. This pulse will not be computed based on the amplitude $\mathcal{E}_x(t)$, but based on a scaled value of $\mathcal{E}_x(t)$. The ramping of the phase will also not be computed based on the amplitude $\mathcal{E}_x(t)$, but on a differently scaled value of $\mathcal{E}_x(t)$. Although theory sets both scale values to one, it appeared that different calibrations give better results. The scale values need to be determined on a daily basis, because they vary even if the qubit transition is tuned to the same frequency. An explanation as to why the optimal scale values differ from theory has yet to be found.

4.3 Determining the resonator frequency

The first step towards controlling the qubit is to determine the resonator frequency. This is achieved by inputting a signal with a constant power of usually −35 dBm into the cavity using the RF signal generator, corresponding to about 0.1 photons in the resonator, taking into account the attenuation due to the microwave transmission line. The output power is measured as a function of the frequency ν_{RF} of the RF signal. This measurement gives, as expected, a Lorentzian function

$$I\frac{\gamma^2}{(\nu_{\text{RF}} - \nu_r)^2 + \gamma^2},$$

which is peaked at the resonator frequency ν_r and has half-width at half-maximum γ and height I. The result of a resonator measurement is shown in Fig. 4.1. In this figure, we extracted the resonator frequency $\nu_r = \omega_r/2\pi = 6.95135\,\text{GHz}$, a quality factor of $Q = \omega_r/\gamma = 2417.08$ and a photon decay rate $\kappa/2\pi = 2.87593\,\text{MHz}$. These parameters were approximately constant over the different experiments since the qubit was always operated at similar transition frequencies. Note that ν_r is not the bare resonator frequency, but the resonator frequency shifted by the presence of the qubit.

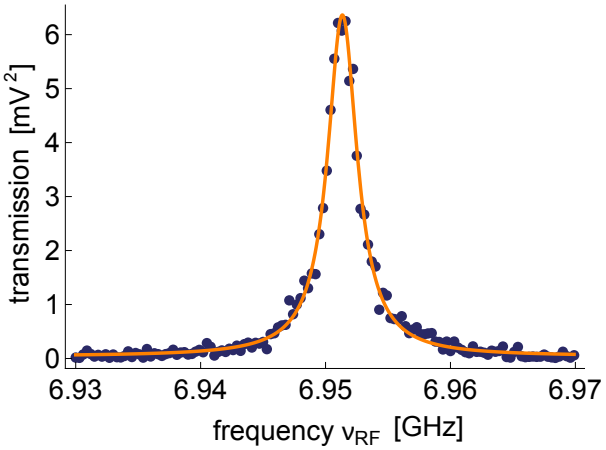

Figure 4.1: Resonator measurement (blue points) and fit (orange line). The plot shows the transmission of the probe signal as a function of its frequency.

4.4 Determining the Rabi frequency

A essential point in qubit manipulation is determining its Rabi frequency. This is achieved as follows:

* Select the kind of pulse which will be used during the experiment, e.g. Gaussian DRAG pulses or DRAG pulses with phase ramping, and set the pulse parameters σ and RF.
* Using pulses with the above specifications, create a sequence of pattern files. A pattern consists of a single pulse with fixed amplitude in resonance with the qubit, $\omega_d = \omega_a$. Throughout the sequence, the amplitude of the pulses is varied from zero to one, one being the maximum output amplitude of the AWG. (We always use the entire power range of the AWG and take care to reduce the power of the signal by introducing adequate damping at a later stage.) The patterns are displayed schematically in Fig. 4.2.
* Run this sequence, performing qubit spectroscopy at the end of each pattern. Repeat the sequence at least 3×10^4 times to accumulate measurement statistics.

A typical measurement outcome of such a sequence is shown in Fig. 4.3. The excited-state population varies between 0 and 1, depending on the pulse area, that is, twice the azimuthal angle by which the state vector was rotated by the pulse. The data is fitted using *Mathematica*. From the fit, one extracts the pulse amplitude which drives the qubit from the ground state into the excited state. A pulse with this precise amplitude is a π-pulse. The pulse with half the amplitude, i.e. which drives the qubit from the ground state into an equal superposition state, is a $\pi/2$-pulse. The visibility, defined as the maximum difference in qubit population observed in a Rabi oscillation experiment, is a parameter to quantify the precision of π-pulses. In this experiment, we obtained a visibility of 1.03 ± 0.01.

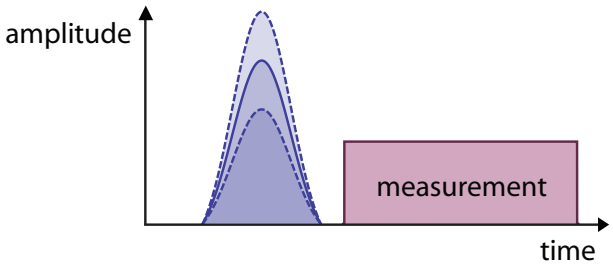

Figure 4.2: Pulse sequence to determine the Rabi frequency. The pulse length is fixed but the amplitude is swept from low to high. The measurement pulse, applied after the Rabi pulse, probes the qubit state.

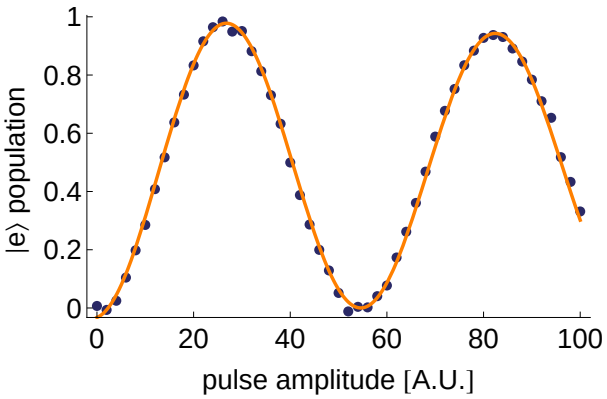

Figure 4.3: Excited state population as a function of pulse amplitude. We see almost two Rabi oscillations, obtained by varying only the pulse amplitude but not the pulse length.

Linearity of Rabi frequency as a function of drive amplitude

To ascertain ourselves that the microwave signals used for manipulating the qubit scale correctly in amplitude, the following experiment was carried out. It is predicted that the Rabi frequency of the qubit is a linear function of resonant drive applied to the qubit [28]. While this is true in an ideal system, power-dependent performance of the microwave components, e.g. the mixer, can cause deviations. The linearity of Rabi frequency as a function of the drive amplitude was tested by exposing the qubit to resonant pulses with square envelopes of variable length, thus producing Rabi oscillations. For a fixed pulse amplitude, the length of the pulse varied in steps of 1 ns. Based on the reconstructed populations, the duration $t_{2\pi}$ necessary for a 2π-pulse and the Rabi frequency were determined. The same procedure was repeated for eight different amplitudes, corresponding to drive frequencies between 10 MHz and 80 MHz. The factor used to convert the pulse amplitudes to drive frequencies, cf. appendix A, was determined using a calibrated DRAG-type $\pi/2$-pulse of length 12 ns. The area covered under the pulse of length $t_{2\pi}$ and amplitude A was computed, too. As can be inferred from eqn. (A.2), the area should amount to unity when the drive amplitude is converted in Rabi frequency.

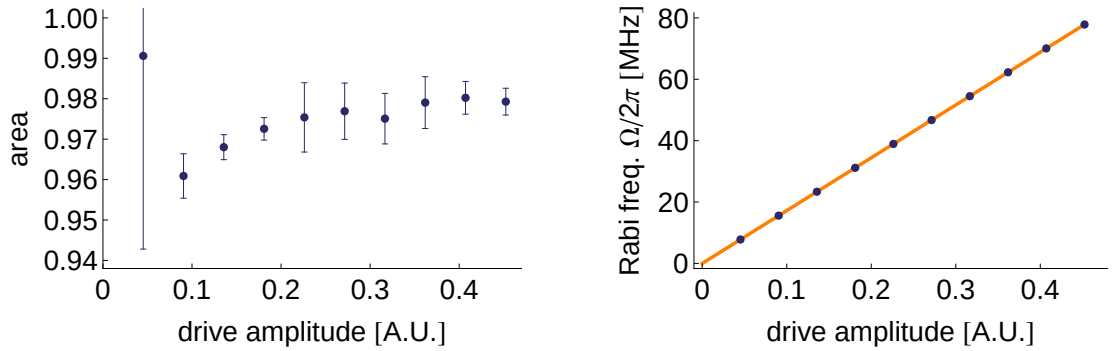

Figure 4.4: **(a)** The area Θ of the pulses which corresponds to a 2π-pulse, plotted as a function of the drive amplitude output by the AWG. In theory, the area should be unity. **(b)** The Rabi frequency $\Omega/2\pi$ increases linearly with the drive amplitude, in keeping with theoretical predictions.

Analysing the collected data, shown in Fig. 4.4, it is apparent that the Rabi frequencies indeed scale linearly with the drive frequencies. The pulse area Θ, however, appears to be 3% to 4% smaller than expected, showing a tendency to increase with the drive. Possible explanations include effects due to the sudden turning-on of the pulse or some non-linearities in the system generating and mixing the pulses. However, the discrepancy, albeit of unclear origin, is hopefully small enough not to be troublesome.

4.5 Ramsey experiment

In order to verify the accuracy of the qubit transition frequency ω_a determined by spectroscopy measurements, one can use a Ramsey interference experiment [16], which bears some similarity to Mach-Zehnder interferometry. Its general operating mode is describe here. Assume the qubit to be initially in the ground state $|g\rangle$. Then, a $\pi/2$ pulse with phase $\varphi = 0$ is applied to qubit, creating a equal superposition state $(|g\rangle - |e\rangle)/\sqrt{2}$. By means of a phase shifting element, this state is transformed into $(e^{i\varphi}|g\rangle - |e\rangle)/\sqrt{2}$. Then, a second $\pi/2$ pulse, again with phase $\varphi = 0$, is applied. The resulting qubit state is

$$\frac{1}{\sqrt{2}}\frac{|e\rangle + |g\rangle}{\sqrt{2}} + \frac{1}{\sqrt{2}}\frac{e^{i\varphi}|e\rangle + |g\rangle}{\sqrt{2}} = \frac{\left(1 + e^{i\varphi}\right)|e\rangle + \left(1 - e^{i\varphi}\right)|g\rangle}{2}.$$

Therefore, the probability of finding the qubit in the ground or in the excited state is

$$P_g = \cos^2\left(\frac{\varphi}{2}\right), \quad P_e = \sin^2\left(\frac{\varphi}{2}\right).$$

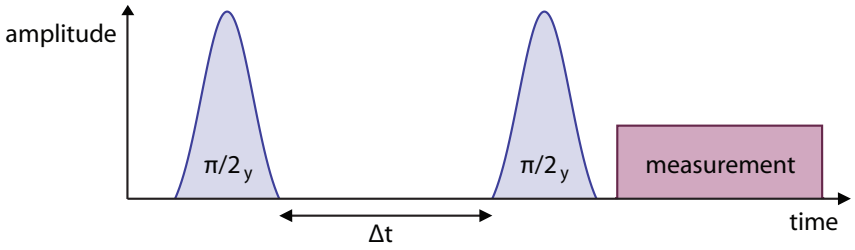

Figure 4.5: A Ramsey pulse sequence. The spacing Δt between the $\pi/2$-pulses is increased in steps of 3 ns.

That is,

$$P_e = \begin{cases} 1 & \text{if } \varphi = 0 \bmod 2\pi, \\ 0 & \text{if } \varphi = \pi/2 \bmod 2\pi \end{cases}.$$

The interpretation is straightforward. In the first case, both $\pi/2$ pulses simply add up and they amount to a single π pulse. In the second case, the state has evolved in such a way that the second pulse undoes the effect of the first pulse and brings the state vector back into the ground state. The implementation of the Ramsey interference experiment is as follows:

* Create a sequence of pattern files. A pattern consists of two $\pi/2$-Rabi pulses, both around the x-axis (i.e. with phase $\varphi = 0$), separated by a time interval Δt. This is illustrated in Fig. 4.5. Both pulses are detuned from the qubit transition frequency by $\Delta = 5$ MHz.
* Throughout the sequence, Δt sweeps the range from 0 to 1500 ns in steps of 20 ns.
* After each pattern, the qubit state is read out. The extracted data is the average obtained from at least 3×10^4 repetitions of the sequence.

Now, the dephasing element comes into play. Consider the qubit in the rotating frame. The first pulse brings $|g\rangle$ into an equal superposition state, regardless of a potential detuning. If the $\pi/2$ pulses are resonant ($\omega_d = \omega_a$), the qubit state will acquire no phase during the interval Δt—it is unaltered. The second pulse then maps the superposition state into $|e\rangle$. If, conversely, the $\pi/2$ pulses are detuned by a frequency Δ, during the interval Δt the qubit will acquire a phase $\varphi = \Delta\,\Delta t$ relative to the drive. Remembering that the second pulse is also applied about the x-axis, it is evident that the second pulse will not bring the superposition state in the excited state since the superposition state has a nonvanishing component along the y-axis. The z-component of the state after the pulse is the y-component of the state right before the pulse. The z-component of the Bloch vector thus reads $\pm\cos\varphi$. This is the component which is measured using qubit spectroscopy. A typical result of a Ramsey experiment is shown in Fig. 4.6, along with a fitted curve. The fitting routine extracts the frequency $\nu = (\tilde{\Delta} + \Delta)/2\pi$ of the oscillations, and the qubit transition frequency is then adjusted by the amount $\tilde{\Delta}$. In this case, we measured oscillations with $\nu = 4.98 \pm 0.01$ MHz.

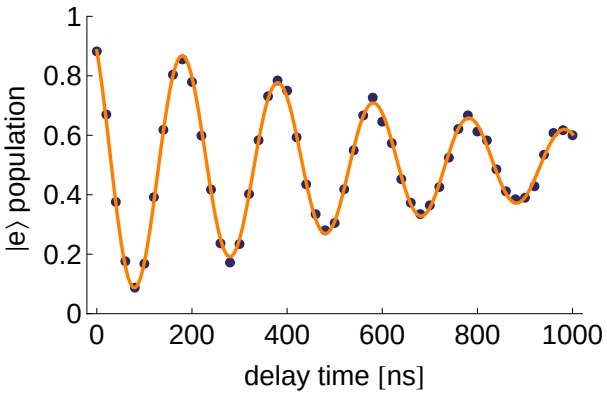

Figure 4.6: Excited-state population as a function of the time delay between the Ramsey pulses. We see Ramsey interference fringes due to off-resonant driving of the qubit. The exponential decay is due to dephasing.

So far, we have not mentioned decoherence. The data in Fig. 4.6 shows that the oscillations are governed by an exponential decay law. There are two types of damping, longitudinal relaxation and transverse relaxation [27], characterised by the decay constants T_1 and T_2. Longitudinal relaxation is essentially population decay, this is why T_1 is called the energy relaxation rate. Transverse relaxation is related to dephasing processes, therefore T_2 is called the dephasing rate. The decay rates associated with T_1 and T_2 are $\gamma_1 = 1/T_1$ and $\gamma_2 = 1/T_2$. They are related via

$$\gamma_2 = \frac{1}{2}\gamma_1 + \gamma_2',$$

where γ_2' is the so-called pure dephasing. The decay rate γ_2 is the decay rate characterising the Ramsey fringes. From the experiment shown in Fig. 4.6, we extracted a dephasing rate $T_2 = 700 \pm 19$ ns using an exponential fit. Comparing this to the fitted T_1, see section 4.1, we see that the main contribution stems from pure dephasing.

4.6 Pulse calibration

Since both spin-echo and state tomography rely crucially on $\pi/2$-pulses, their exact calibration is of utmost importance. Amongst the factors contributing to imprecisions is (a) the difficulty of accurately determining the amplitude needed for producing a π pulse, (b) variations in the qubit transition frequency as well as (c) the question whether a 90-phase-shifted pulse about the x-axis is a pulse about exactly the y-axis or is slightly off due to mixer inaccuracies (which should be calibrated).

Point (a) is discussed in section 4.4. In order to verify point (b), that is, to detect possible fluctuations in the transition frequency, repeated qubit spectroscopy measurements were performed during approximately 12 hours. In total, 313 measurement sequences determining both

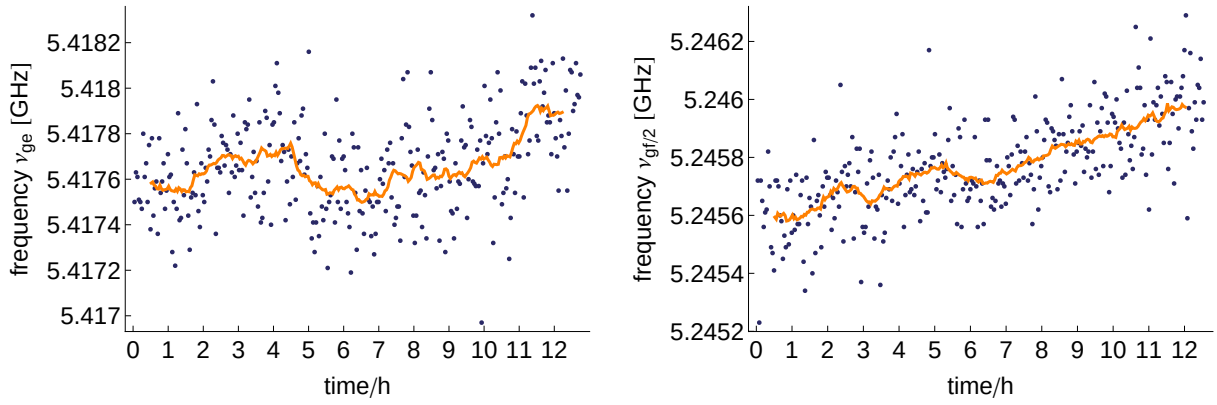

Figure 4.7: The plots display successive measurements of ν_{ge} (left) and $\nu_{gf}/2$ (right). The fluctuations of the transition frequencies stay within a frequency band of about 400 kHz. The data was acquired continuously during about 12 hours.

$\nu_{ge} = \omega_{ge}/2\pi$ and $\nu_{gf}/2 = (\omega_{gf}/2)/2\pi$ were performed. The transitions were located approximately at $\nu_{gf}/2 \approx 5.418\,\text{GHz}$ and $\nu_{ge} \approx 5.245\,\text{GHz}$. A sequence consists of two spectroscopy sweeps across the frequencies from 5.216 GHz to 5.450 GHz in steps of 500 kHz, so as to see both transitions. The power of the spectroscopy signal during the first sweep is −42 dBm (to observe the $|g\rangle \rightarrow |e\rangle$-transition), during the second sweep it is −10 dBm (to observe the $|g\rangle \rightarrow |f\rangle/2$-transition). For each transition, the power was chosen low enough to guarantee a narrow lineshape but high enough to ensure a peak value markedly above the background.

The results of the repeated measurement of the transition frequencies are shown in Fig. 4.7. The transition frequencies were extracted from the data using a Lorentzian fitting routine. The average transition frequencies are $\nu_{ge} = 5.41766 \pm 0.00021$ and $\nu_{gf}/2 = 5.24577 \pm 0.00017$. Whereas $\nu_{gf}/2$ increased by approximately 350 kHz over the thirteen hours the measurement lasted, ν_{ge} remains in a frequency band of about 200 kHz. The expected charge dispersion ϵ_i for the ith level can be calculated using eqn. 2.12. One finds 65 kHz for the e-level and 2.38 MHz for the f-level. This suggests that the drift is not caused by charge dispersion only. Still, the drift in the transition frequency ν_{ge} is negligible for the geometric phase experiment since it causes a shift in Rabi frequency which lies within measurement inaccuracy. The charge dispersion of the f-level, however, would play a role in experiments making use of the thrid level.

As far as (c) is concerned, a purely pragmatic approach was taken. We first determined the amplitude needed for the Rabi pulses as explained above in section 4.4. Then, a sequence of calibration pulses was applied to the qubit. In the sequence, there are three types of patterns. There are patterns with pulses which transport the qubit form the ground state into (1) the excited state, (2) an equal superposition state, (3) the ground state. For each type of pulses, the axis along which the qubit is rotated is varied. In the experiment, the first sequence of pulses was applied using the Rabi pulse amplitude. Then, both the π and $\pi/2$ amplitudes were

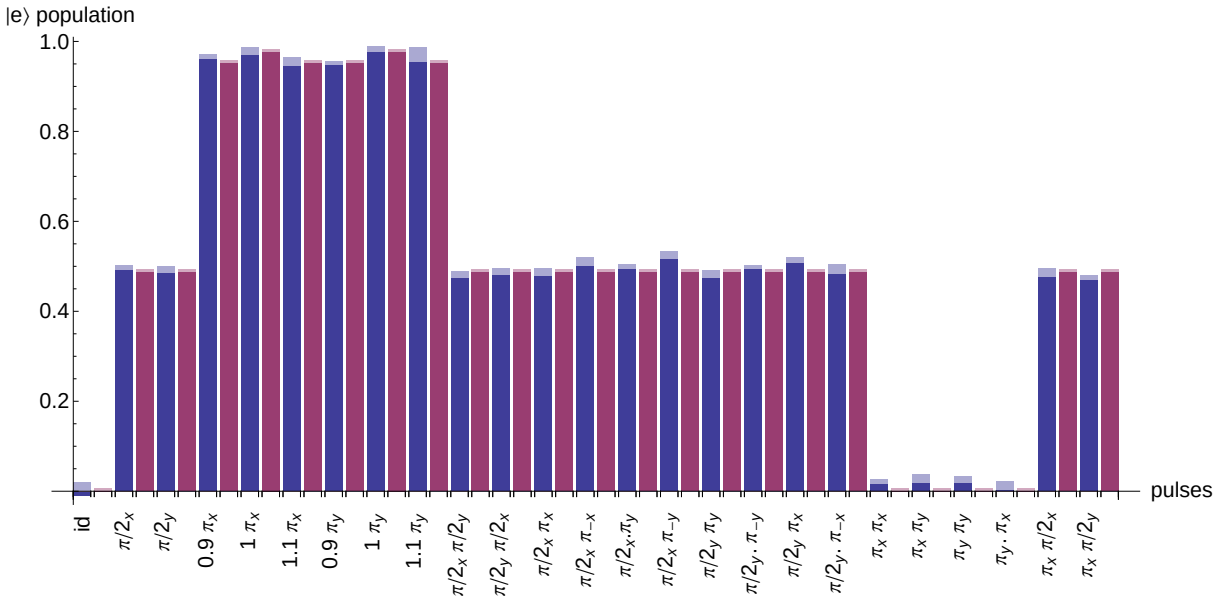

Figure 4.8: Results of the calibration sequence. The blue bars refer to the experimental results, the light blue bars on top indicates the standard deviation. The red bars indicate the population expected theoretically, mutliplied with the maximum population measured after a π-pulse. The light red bars indicate the errors of population reconstruction.

modified until the the correspondence between the expected population and the measured populations was satisfactory.

It is to be noted that the calibration of the pulses where a excited state population of $P_{e,z} = 1/2$ is expected is more difficult than the calibration of the pulses where one expects $P_{e,z} = 1$. This is because the expected population goes as $\frac{1}{2}(1 - \cos r\pi)$, where r it the ratio of the pulse to a π-pulse. [E.g. $\alpha = 1$ is a π-pulse, $r = 1/2$ is a $\pi/2$-pulse.] That is, when $r \approx 1$, the excited state population $P_{e,z}$ is insensitive to r because the cosine is approximately constant, whereas when $r \approx 0.5$ the cosine varies the most quickly and $P_{e,z}$ becomes sensitive to fluctuations in r.

If the results of a calibration were not satisfactory, it was repeated with slightly different scaling values of the DRAG pulses, see 4.2. Experience shows that the calibration pulses give unreliable results if the number of averages is too low. The results shown in Fig. 4.8 were obtained using pulses with phase-ramping of length 20 ns, with $\sigma = 5$ ns and $t = 2$. The sequence was run fifteen times, totalling 150×10^3 averages. This calibration was judged satisfactory and used for measurements of the geometric phases. It is to be noted that the pulses do not attain population levels of $0, 0.5$ and 1 because the pulse length is finite: the state starts to decay even before the pulse is over. This accounts in particular for the non-vanishing populations measured in the 6^{th}, 5^{th} and 4^{th} last pulses.

4.7 State tomography

How are we to gain information about the phase of the qubit? To determine the phase, full knowledge of the qubit state is indispensable. Quantum state tomography, or state tomography for short, is the process of experimentally determining the state of an unknown quantum state [14]. Remembering that any qubit state can be decomposed as $\rho = \frac{1}{2}(\mathrm{id}_2 + r_x\sigma_x + r_y\sigma_y + r_z\sigma_z)$, cf. eqn. (2.4), it appears that knowledge of r_x, r_y and r_z is sufficient. But, since the measurement setup permits only the measurement of the z-component of the qubit r_z, how are we to find out the other components?

In this paragraph, we describe how to gain full knowledge of the state. The procedure relies on the principle that, given identical experimental conditions, all reiterations of the same experiment will yield the same results. By repeating the sequence and reading out a different component each time, one gains information about r_x, r_y and r_z. This is achieved by rotating the qubit just before the readout procedure. A tomography sequence consists of four consecutive repetitions of the sequence that manipulates the qubit. What differs between the repetitions is the very end of the patterns. At the end of the first sequence, no additional pulse follows. At the end of the second (third) sequence, however, there is one additional $\pi/2$-pulse around the x-axis (y-axis). At the end of the fourth sequence, there is a π-pulse around the x-axis. The effect of those pulses is to rotate the qubit state vector. After each of those four sequences, the z-component of qubit state is read out. The first readout gives r_z, the second readout gives r_x and the third readout r_y. The fourth readout gives the ground state population. In theory, the sum of the ground and excited populations should add up to one. If this is not the case, either the pulse calibration is imprecise or there is population in higher levels. This is why the fourth readout serves as a consistency check.

4.8 Spin-echo

No attempts were made to measure the total accumulated phase of the qubit, i.e. the sum of the geometric and dynamic contributions, and compute the dynamical part to obtain the geometric part. Instead, we used a technique called spin-echo [52], which was developed in the field of nuclear magnetism to restore transverse magnetisation. In essence, a spin-echo sequence is a Ramsey sequence with an additional π-pulse placed symmetrically in between the two $\pi/2$-pulses. The pulse sequence is illustrated in Fig. 4.10. It has two effects. First, it has been shown that the dephasing time T_2^* of a spin-echo sequence can be larger than the T_2 extracted from a Ramsey experiment [29]. Second, it cancels out the dynamical phases the qubit accumulates during the free evolution between the $\pi/2$-pulses, because the π-pulse flips the sign of the dynamical phase. This can be seen in Fig. 4.10. A T_2^*-measurement was carried out using 12 ns pulses with phase ramping, driving the qubit at resonance. The data and the corresponding fit are depicted in Fig. 4.9. We extracted $T_2^* = 586 \pm 14$ ns, which is about 100 ns shorter than the conventional T_2. For this transmon sample, the spin-echo procedure does not reduce dephasing.

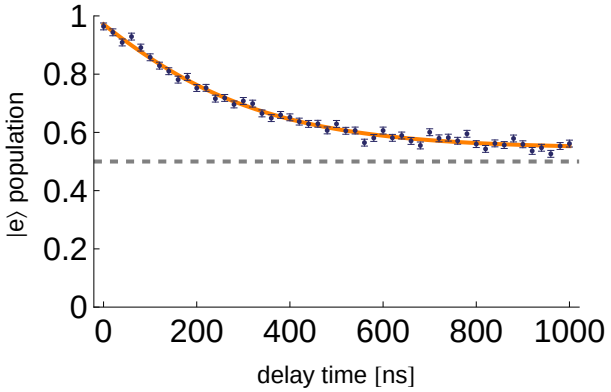

Figure 4.9: Populations measured after the spin-echo sequence. The populations shows exponential decay as a function of the time between the pulses. Asymptotically, p_e approaches one-half.

In practice, the π-pulse can be implemented around any axis lying in the (x, y)-plane, orthogonal to the quantisation axis, the z-axis. The pulse pattern shown in Fig. 4.10, that is $\frac{\pi}{2}|_y, \pi|_x, \frac{\pi}{2}|_y$, puts a qubit that was initially in the ground state into the excited state. The sequence $\frac{\pi}{2}|_y, \pi|_y, \frac{\pi}{2}|_y$, on the other hand, transports the qubit from the ground state back into the ground state. The following paragraphs describe how this was verified experimentally.

Rotating the π-pulse. A sequence of spin-echo patterns with variable rotation axes of the π pulse was implemented. The rotation axis of the π-pulse was varied in steps of 5° from −180° (negative x-axis) over −90° (negative y-axis) over 0° (positive x axis) to 175°, whereas both $\pi/2$-pulses were applied around the y-axis. For prefect pulses, the theory predicts populations $\langle\sigma_y\rangle = -\sin k$ and $\langle\sigma_z\rangle = \cos k$, where k is the angle of the rotation axis of the π-pulse. The pulse patterns are akin to the spin-echo patterns shown in Fig. 4.10, the variable rotation axis of the central pulse being the only difference.

The pulses used were pulses with phase-ramping of length 12 ns. The experiment was repeated with two different pulse separation times Δt. Every datapoint was averaged about 65000 times. The result of a sequence with $\Delta t = 200$ ns, displayed in Fig. 4.11, are in good accordance with theory. Averaged over the six repetitions of the experiment, the phase offsets are $(1.9 \pm 2.6)°$ for σ_y and $(2.3 \pm 2.4)°$ for σ_z. Averaged over the ten repetitions of the experiment with $\Delta t = 100$ ns, the offsets amount to $(0.8 \pm 0.4)°$ for σ_y and $(1.5 \pm 0.4)°$ for σ_z. These offsets are too small to account for potential deviations in the Berry phase measurement.

Adding supplementary dynamic evolution. As mentioned in the introductory paragraph of this section, the spin-echo technique cancels the phase the qubit acquires during the free evolution between the Ramsey pulses. It is, in fact, more powerful: since the π-pulse inverts the sign of the dynamical phase, any kind of dynamic phase can be cancelled as long as the evolution of the qubit is identical before and after the π-pulse. We exploit this property in this experiment by subjecting the qubit to identical adiabatic pulses between the spin-echo pulses. The qubit is driven with constant detuning. After the first $\pi/2$-pulse, we increase the drive field adiabati-

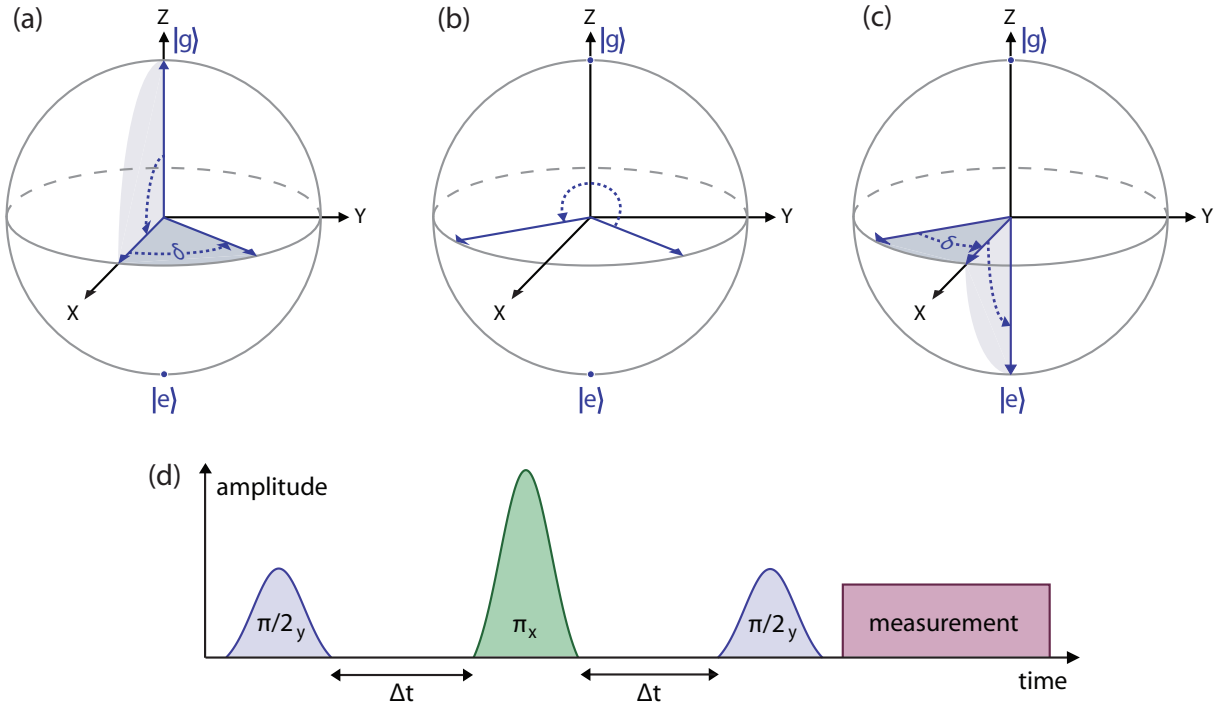

Figure 4.10: The evolution of the state vector during a spin-echo sequence, (a-c), and the pulses used to produce it, (d). **(a)** The state vector is first rotated by $\pi/2$ about the y axis and then acquires a dynamical phase δ during the time Δt. **(b)** The π-pulse about the x axis mirrors the y component of the state vector. **(c)** After yet another interval Δt, the state vector is parallel to the x-axis. Finally, a $\pi/2$-rotation about the y-axis maps the state vector to the ground state. **(d)** A spin-echo pattern. The two $\pi/2$-pulses about the y-axis are placed symmetrically in time before and after the central π-pulse about the x-axis. The time interval is Δt.

cally, applying it on the $\mathcal{E}_x$-quadrature only. Then, the field is kept constant for a determined amount of time before the qubit is adiabatically ramped back to zero drive field. After the spin-echo π-pulse, the ramping procedure is repeated. The pattern is concluded by the spin-echo $\pi/2$-pulse. It is depicted in Fig. 4.12.

The applied drive corresponded to 1.3 times the amplitude of a $\pi/2$-pulse and the spacing Δt between the spin-echo pulses was 200 ns. The results of a measurement with 65535 averages per data point are displayed in Fig. 4.13. The experiment was repeated five times, leading to phase shifts $(-2.4 \pm 1.3)^\circ$ for σ_y and $(-0.4 \pm 0.6)^\circ$ for σ_z, closely matching the theory.

In conclusion, the deviations from the expected is not large enough to account for potential deviations measured in spin-echo measurements. Significant deviations would have introduced errors in the read-out of the populations $\langle\sigma_y\rangle$ and $\langle\sigma_z\rangle$. These errors would in turn have given rise to inaccuracies in the measured geometric phase.

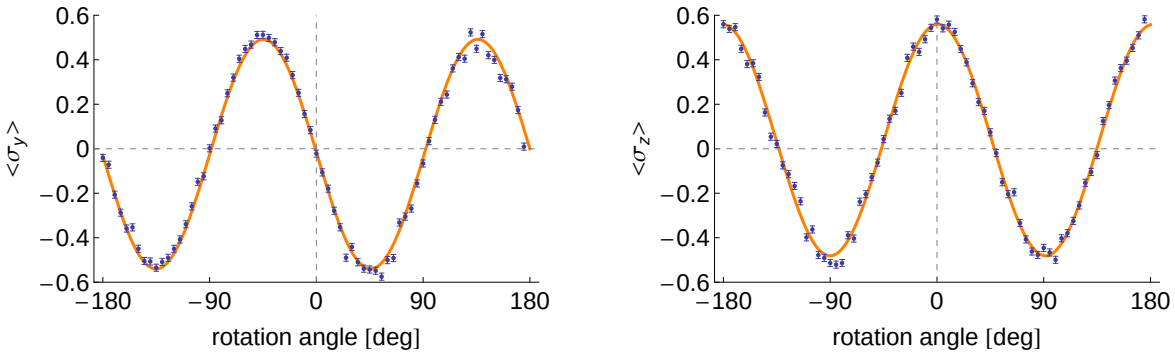

Figure 4.11: Populations $\langle\sigma_y\rangle$ and $\langle\sigma_z\rangle$ after spin-echo sequences with variable rotation axis of the π-pulse, reconstructed using state tomography. The short pulses belonging to the spin-echo sequence were $\Delta t = 200\,\text{ns}$ apart. The orange lines are fits to the data, from which the shifts in phase of the curves with respect to the theory curves can be computed. The phase shift is 2.3° in (a) and 3.3° in (b), showing good agreement with theory.

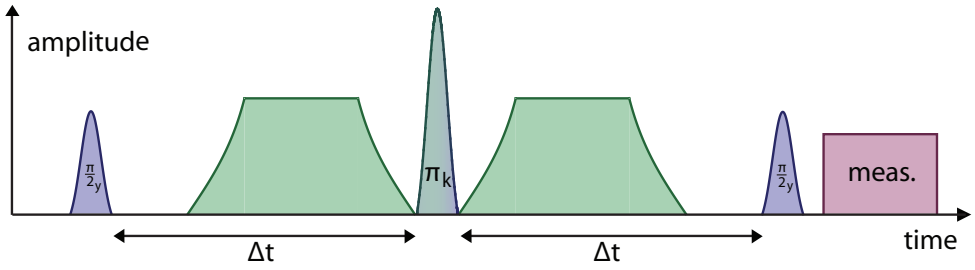

Figure 4.12: The additional pulses (green) in between the spin-echo pulses induce adiabatic qubit motion. Since they are repeated symmetrically on either side of the central π_k-pulse, the qubit acquires no dynamic phase during this sequence if its motion is completely adiabatic.

4.9 Measurement of Berry's phase

This section presents the central results of the thesis, the measurements of Berry's phase. It is organised as follows. First, we describe the paths the qubit traces out and how it acquires a geometric phase. Then, we present the implementation of the pulses used to manipulate the qubit and the results we expect. Finally, after considerations on adiabaticity, a discussion of the analysed data concludes the section.

Qubit path

In this paragraph, we describe the path that the qubit Hamiltonian traces out in parameter space so that the qubit acquires a geometric phase. The general idea is the following: the qubit

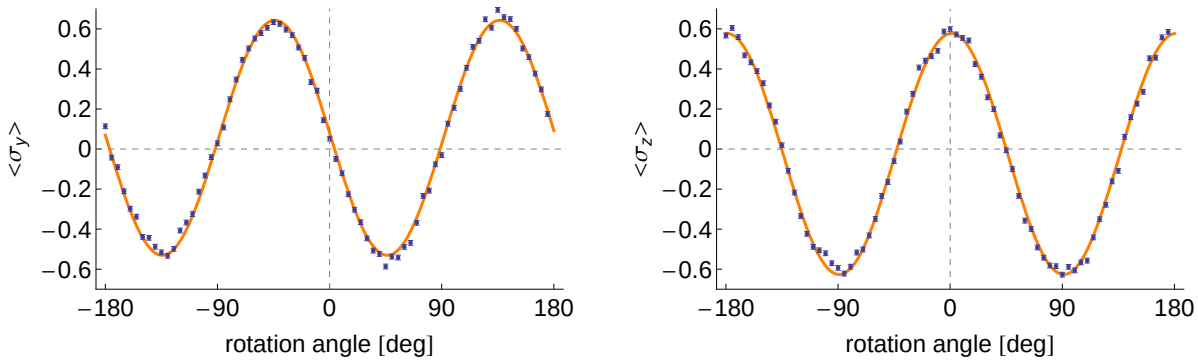

Figure 4.13: Populations $\langle\sigma_y\rangle$ and $\langle\sigma_z\rangle$ (measured with state tomography) after spin-echo sequences with variable rotation axis of the π-pulse and adiabatic motion of the qubit, as depicted in Fig. 4.12. The pulse separation was $\Delta t = 200\,\text{ns}$. In between the orange lines are fits to the data, from which the shifts in phase of the curves with respect to the theory curves can be computed. The phase shift is $-2.1°$ in (a) and $0.3°$ in (b), close to the theoretical predictions.

follows the path indicated in Fig. 4.14a *twice*. Depending on the orientation of the contours, its wavefunction will acquire different phases. If the qubit traverses the contour C^+, it acquires a phase $\gamma_\text{d} + \gamma_\text{g}$. On the other hand, if it traverses C^-, it acquires a phase $\gamma_\text{d} - \gamma_\text{g}$, since only the geometric phase depends on the orientation of the loop. We make use of the spin-echo technique, so that the dynamic phases accumulated along each contour cancel exactly.

The pulse patterns used to measure the geometric phase start by creating an equal superposition state by means of a $\pi/2$-pulse applied to the ground state.

$$|g\rangle \xrightarrow{\frac{pi}{2}|_y} \exp\left\{\mathrm{i}\frac{\pi}{2}\frac{\sigma_y}{2}\right\}|g\rangle = \frac{1}{\sqrt{2}}\left(\cos\left(\frac{\pi}{4}\right)|g\rangle + \sin\left(\frac{\pi}{4}\right)|e\rangle\right) = \frac{|e\rangle + |g\rangle}{\sqrt{2}}.$$

Then, the qubit traverses two contours $C^\pm$ separated by a spin-echo π-pulse. As an example, we consider the pattern C^{+-}, in which the contour C^+ is traced out before the contour C^-. The state vector after traversing the first loop C^+ may be expressed as [53] $(|g\rangle + \mathrm{e}^{2\mathrm{i}(\gamma_\text{d}+\gamma_\text{g})}|e\rangle)/\sqrt{2}$. The π-pulse about the x-axis inverts the sign of the phase and the state vector reads $(|g\rangle + \mathrm{e}^{-2\mathrm{i}(\gamma_\text{d}+\gamma_\text{g})}|e\rangle)/\sqrt{2}$. Traversing the second loop C^- contributes $\gamma_\text{d} - \gamma_\text{g}$ to the phase of the $|e\rangle$ component of the state vector. Therefore, the state reads

$$(|g\rangle + \mathrm{e}^{2\mathrm{i}(\gamma_\text{d}-\gamma_\text{g})}\mathrm{e}^{-2\mathrm{i}(\gamma_\text{d}+\gamma_\text{g})}|e\rangle)/\sqrt{2} = (|g\rangle + \mathrm{e}^{-4\mathrm{i}\gamma_\text{g}}|e\rangle)/\sqrt{2}.$$

Similarly, after traversing the first contour clockwise and the second contour anticlockwise, C^{-+}, the state vector reads $(|g\rangle + \mathrm{e}^{+4\mathrm{i}\gamma_\text{g}}|e\rangle)/\sqrt{2}$. The pulse pattern ends with a $\pi/2$-pulse, which concludes the spin-echo sequence.

The full-blown experiment, i.e. a spin-echo pattern followed by state tomography, consists of four fast pulses: three for the spin-echo pattern and one for tomography. However, the last

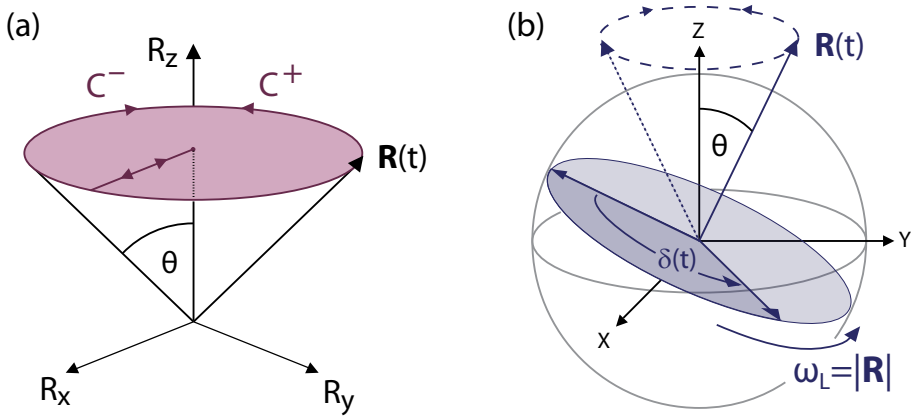

Figure 4.14: **(a)** The path traced out by the state vector in parameter space. At first, there is only detuning, orienting **R** along R_z. Then, as drive increases, it acquires an new component along R_x. After the drive has reached its maximum value, the drive amplitude is kept constant and **R** forms an angle ϑ with respect to the R_z-axis. Then, the phase of the drive is modulated, causing **R** to trace out the path $C^{\pm}$. Finally, the drive amplitude is decreased again and **R** points along R_z, as in the beginning. **(b)** The state vector s in the rotating frame, while detuning and drive are being applied. The qubit is precessing around the axis $\mathbf{R}(t)$ with Larmor frequency $\omega_L = |\mathbf{R}(t)|$. As the drive amplitude changes, so does the orientation of the axis: during one cycle $C^{\pm}$, the axis traces out the path indicated by dashed lines. Graphic adapted from [29].

pulse is dispensable since two consecutive $\pi/2$-pulses (around x,y,z) only change the order in which the components r_i are read out in state tomography. So, at the minute cost of rotating the measured data to compensate for the missing Ramsey $\pi/2$- pulse, the sequence is shorter and decoherence effects are lessened. Also, the data is more accurate since every additional $\pi/2$-pulse introduces some imprecision.

Implementation of the pulses

By means of detuned microwave pulses, the qubit is subject to an effective pseudo-magnetic **B**-field **R**, whose components are $(\mathcal{E}_x, \mathcal{E}_y, \Delta)$, see section 2.5. By skilfully manipulating the amplitude and phase of the microwave pulses, the state vector is caused to follow the paths $C^{\pm\pm}$. An example of a pulse sequence is shown in Fig. 4.15. After the resonant $\pi/2$-pulse, the drive field is ramped up adiabatically. The detuning Δ is kept fixed at all times. Ramping the drive field tilts **B**: from being parallel to the z-axis, $\mathbf{B} = (0, 0, \Delta)$, it is brought to $\mathbf{B} = (\mathcal{E}_x, 0, \Delta)$ and forms an angle ϑ with respect to the z-axis. This angle is called the opening angle, and its cosine is $\cos\vartheta = \Delta/\sqrt{\Delta^2 + \Omega^2}$. Since the magnetic field is ramped up slowly, the plane in which superposition state lies remains perpendicular to **B**. When the drive is ramped up completely, we increase the phase of the microwave drive linearly. This causes **B** to rotate around the z-axis, either clockwise or anticlockwise. Again, this happens at adequately low speed to ensure adiabaticity (cf. next paragraph). Then, after a full rotation, the drive field is ramped back

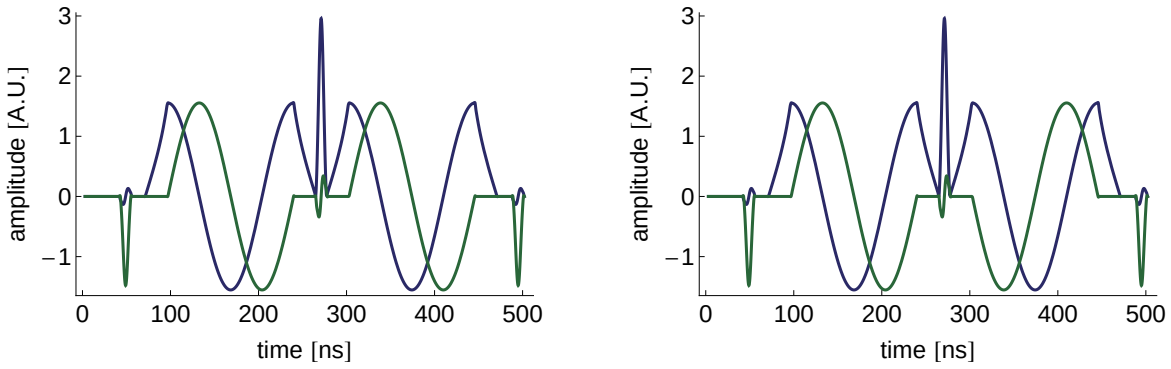

Figure 4.15: Depiction of the envelopes of the pulses applied during a Berry phase measurement. The blue line corresponds to the $\mathcal{E}_x$-quadrature, whereas the green line corresponds to the $\mathcal{E}_y$-quadrature of the applied microwave pulse. Subjected to the pulse sequence to the left, the qubit traces out the path C^-, is then flipped around the x-axis and traces out the same C^-path once more. That is, the qubit follows the path C^{--} and both the geometric and the dynamic phases cancel out. In the pulse sequence to the right, the $\mathcal{E}_y$-quadrature after the π-pulse is phase-shifted by 180°. This inverts the direction in which the second path is traversed. Therefore, the qubit follows the path C^{-+} and acquires a geometrical phase.

again. After applying the π-pulse, the qubit is made to trace out the second contour. A state tomography pulse, also acting as spin-echo-pulse, concludes the sequence.

In the limit of total adiabaticity, the expected excited-state populations $\langle P_e \rangle$ for the contour C^{-+} are

$$\langle P_{e,x} \rangle = 0, \quad \langle P_{e,y} \rangle = \frac{1}{2}(1 - \sin\varphi), \quad \langle P_{e,z} \rangle = \frac{1}{2}(1 - \cos\varphi).$$

Therefore, since the populations and the components of the state vector are related via $\mathbf{r} = 1 - 2\mathbf{P}_e$, we expect

$$\langle \sigma_x \rangle = 0, \quad \langle \sigma_y \rangle = \sin\varphi, \quad \langle \sigma_z \rangle = \cos\varphi.$$

From this, the phase can readily be extracted as $\varphi = \arctan\langle \sigma_y \rangle / \langle \sigma_z \rangle$.

A note on the amount of geometric phase the qubit acquires during a full pattern: according to section 2.6, the accumulated phase is

$$\gamma_g(C^\pm) = \mp\frac{1}{2} i\alpha(C^\pm). \tag{4.1}$$

That is, the geometric phase is half the solid angle α subtended by the contour $C^\pm$ traced out by $\mathbf{R} = (\mathcal{E}_x, \mathcal{E}_y, \Delta)$, see Fig. 4.14a. The solid angle is $\alpha = 2\pi(1 - \cos\vartheta)$, where ϑ is a function of the drive and the detuning. However, the experiment is designed in such a way that the qubit acquires a phase φ which is the *double* of the α. The factor four has two causes. Firstly, the phase γ_g is accumulated twice because two contours are traversed in a measurement. Secondly, the Ramsey interferometry also doubles the acquired phase. In brief, we expect to measure $\varphi = 2\alpha$.

Considerations on adiabaticity

When measuring Berry's phase, adiabaticity must be maintained during all pulses except the (resonant) π- and $\pi/2$-pulses. A measure of adiabaticity is the adiabaticity parameter $\mathcal{A}$. It is defined as the ratio of the rate of change of the state vector $\mathbf{r}(\vartheta(t), \varphi(t))$ and the Larmor precession frequency $\omega_\mathrm{L} = \sqrt{\mathcal{E}^2 + \Delta^2}$ in the rotating frame:

$$\mathcal{A} = \frac{|\dot{\mathbf{r}}|}{\omega_\mathrm{L}} = \frac{\sqrt{(\dot{\vartheta}\,\cos\vartheta\,\cos\varphi - \dot{\varphi}\sin\vartheta\,\sin\varphi)^2 + (\dot{\vartheta}\,\cos\vartheta\,\sin\varphi + \dot{\varphi}\sin\vartheta\,\cos\varphi)^2 + (\dot{\vartheta}\,\sin\vartheta)^2}}{\sqrt{\mathcal{E}(t)^2 + \Delta^2}},$$

where $\mathbf{r}$ is the Bloch vector. In the special case where φ is constant, i.e. when the drive field is ramped up, the adiabaticity parameter reduces to

$$\mathcal{A} = \frac{|\dot{\vartheta}|}{\sqrt{\mathcal{E}(t)^2 + \Delta^2}}.$$

When, on the other hand, ϑ is constant, e.g. when the drive field is rotated around the z-axis, one has

$$\mathcal{A} = \frac{|\dot{\varphi}\,\sin\vartheta|}{\sqrt{\mathcal{E}(t)^2 + \Delta^2}}.$$

In the measurement sequences, $\mathcal{A}$ is being kept smaller than 0.04. This proved to be low enough to obtain good results. Measurements were performed with $\mathcal{A} \leq 0.025$ during the part of the pulse sequence where the drive amplitude is varied and slower motion of the qubit during the part of the pulse sequence where the phase of the drive is varied. However, in this regime of adibaticity, both measurements gave similar results.

Collected data and extracted phases

Early attempts at measuring the geometric phase with drive pulses which did not have constant adiabaticity but the envelope of a hyperbolic tangent function turned out to be unsuccessful. The control measurements (performed by having the qubit trace out the path C^{++} for example) showed that the qubit acquired a non-zero geometric phase. At this stage, the π- and $\pi/2$-pulses were Gaussian pulses without DRAG compensation. After implementing adiabatic ramping, we tried to repeat the experiment with Gaussian pulses without DRAG compensation. The obtained phases showed marked improvement, although the deviations from theoretical predictions were still important. This is why, in a next step, DRAG pulses were used. The greatest improvement, however, was achieved by using pulses with phase ramping.

Experiments with $\Delta/2\pi = -50\,\mathrm{MHz}$.— The measurements shown in Fig. 4.16 were performed using 12 ns-pulses with phase ramping for the direct pulses. The adiabaticity coefficient is $\mathcal{A} \leq 0.04$ and the detuning is $\Delta/2\pi = -50\,\mathrm{MHz}$. To accumulate measurement statistics, every datapoint was averaged 6.5×10^5 times. The drive was increased from approximately 2 MHz to 78 MHz, resulting in opening angles ϑ from 0° to 29°. For each fixed drive amplitude, two

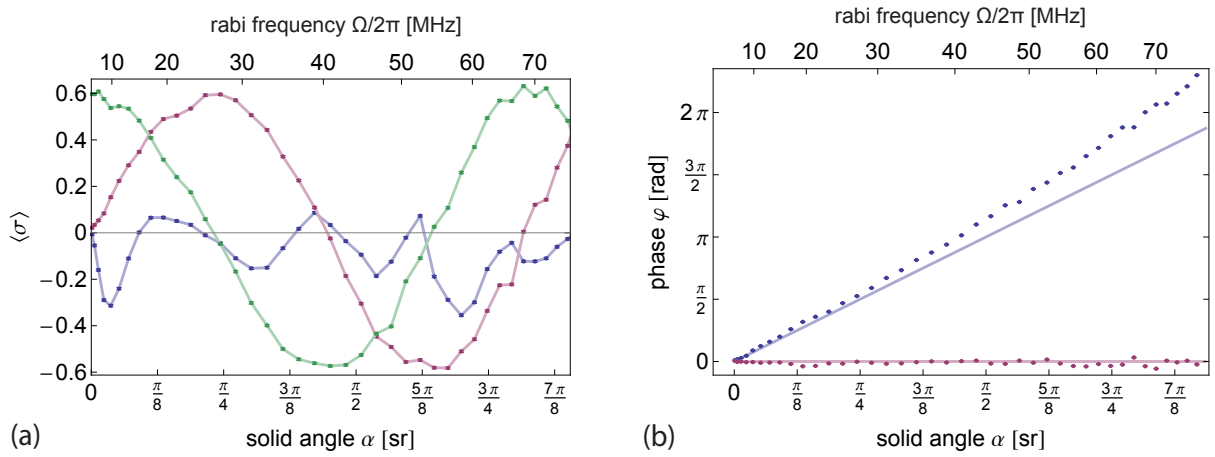

Figure 4.16: **(a)** Measured components $\langle\sigma_x\rangle$, $\langle\sigma_y\rangle$ and $\langle\sigma_z\rangle$ (blue, red and green) of the state vector after qubit evolution along the path C^{-+}. The oscillations of $\langle\sigma_x\rangle$ are due to non-adiabatic effects. The detuning was $\Delta/2\pi = -50\,\text{MHz}$. The data points are connected to facilitate reading the graph. **(b)** The blue curve is the phase extracted from the data shown in (a). The red curve is the phase obtained in the zero-phase control measurement which was carried out simultaneously. In the control measurement, the qubit followed the path C^{++}. The solid lines are theory curves as predicted by Berry. The data shows a root-mean-square deviation of 0.42 rad (C^{-+}) and 0.06 rad (C^{++}) from the respective theory lines.

pulse patterns were applied: the first one causing the qubit to trace out the contour C^{-+}, the second one C^{--}. The second measurement serves as a control measurement in which the qubit should accumulate no phase at all. A pattern has a length of roughly 500 ns. Dephasing effects reduce the visibility of the measured state vector to 59%.

Experiments with $\Delta/2\pi = 30\,\text{MHz}$.— With a lower detuning and otherwise unchanged parameters, the pulse sequence is lengthened to some 700 ns because ramping the drive takes more time (if one keeps the adiabaticity parameter constant). This implies a further reduction of the visibility. We carried out a measurement with a detuning of $\Delta/2\pi = 30\,\text{MHz}$. The extracted geometric phase is shown in Fig. 4.17b. The visibility amounts to 50%. In Fig. 4.17a, the results of a measurement with $\Delta/2\pi = 50\,\text{MHz}$ are shown for comparison. Only the detuning was modified, the other paramters were not changed. The data suggests that the phase measurement is more accurate for smaller detunings.

Concluding remarks

The measurements of Berry's phase show good agreement with theory for small opening angles ϑ. However, above a certain value, the phase departs from the Berry's prediction. When this occurs, and on which parameters it depends, is as yet unknown. The control measurements, which match the theory even for large drive amplitudes, show that the spin-echo technique works well. This was also confirmed by the measurements in section 4.8. We do not expect

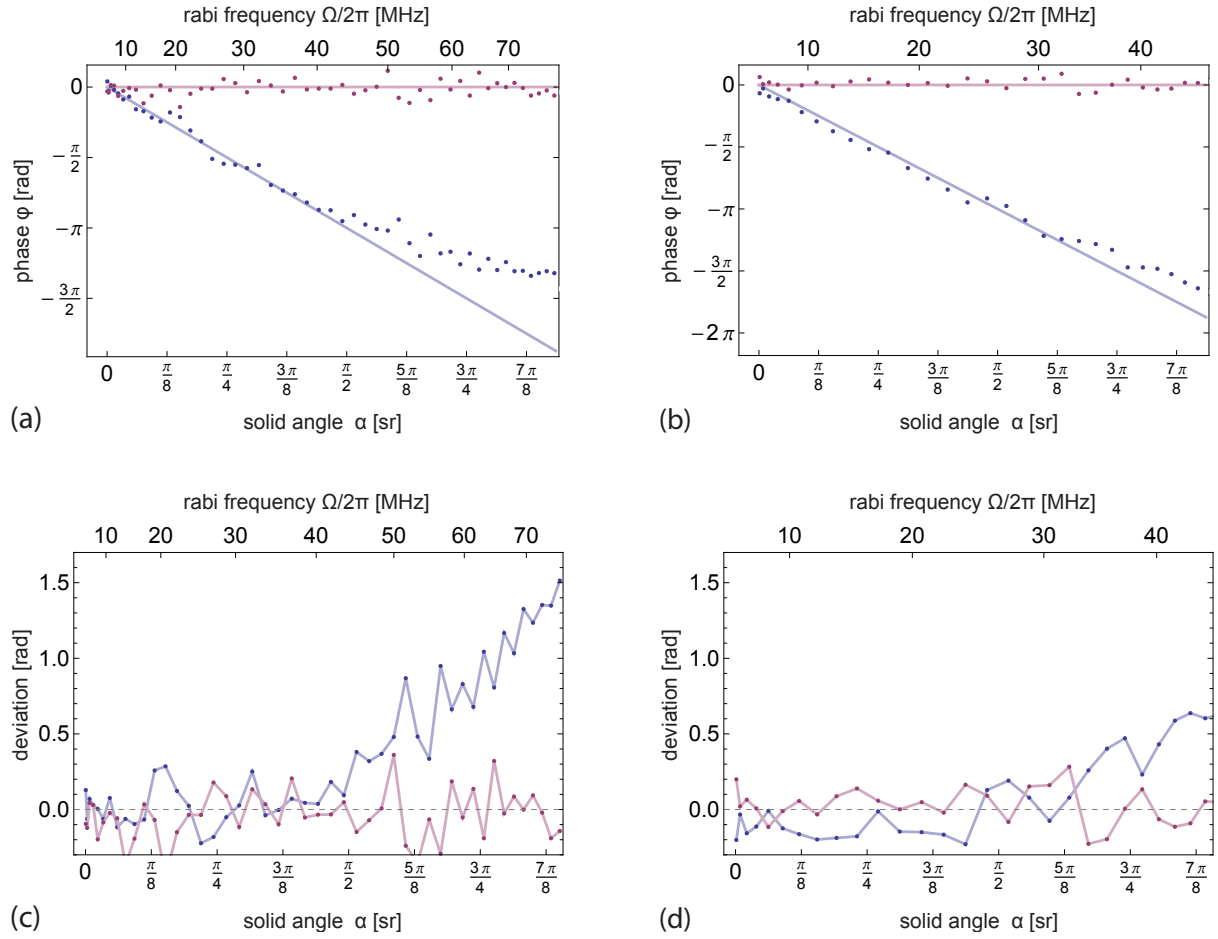

Figure 4.17: Geometric phases measured with different detunings and the deviations from theory. The blue curves stem from C^{+-} measurements, the red curves from C^{--} control measurements. The solid lines in (a) and (b) are theory curves. **(a)** The detuning is $\Delta/2\pi = 50\,\mathrm{MHz}$ and each data point was averaged 65000 times. The root-mean-square deviations from theory are 0.70 rad for C^{+-} and 0.17 rad for C^{--}. **(b)** The detuning is $\Delta/2\pi = 30\,\mathrm{MHz}$ with tripled averaging (195000 times). The root-mean-square deviations from theory are 0.30 rad for C^{+-} and 0.12 rad for C^{--}. **(c)** Deviations of the measured phases in (a) from the theory line. **(d)** Deviations of the measured phases in (b) from the theory line.

sudden changes in the transition frequency ω_a of the qubit either. The stability of the transition frequencies over a long period of time was demonstrated in section 4.6. Therefore, also this influence can be ruled out. Furthermore, in the same section, we showed that the π-pulses are well calibrated. The calibration was verified before and after measurements of Berry's phase and the results strongly suggest that no deterioration occurs during the measurements.

The chosen detuning plays a important role in the measurement of the geometric phase. Comparison of Fig. 4.17a and Fig. 4.17b shows that the phase measured with the lower detuning agrees better with theory. An explanation for this fact has yet to be found. Moreover, it seems somewhat surprising that the Berry phase measurement with a negative detuning, see Fig. 4.17a, agrees about as well with theory than the measurement with opposite detuning, 4.16b. If the detuning is positive, the drive frequency is below the qubit transition frequency ω_{ge}. Since the qubit has a negative anharmonicity, drive with positive detuning is closer to the transition frequency ω_{ef}. Therefore, one would expect more unwanted population in the higher level with positive than with negative detuning.

Although Berry's phase was measured successfully within a broad range of drive frequencies (≈ 80 MHz), a rigorous explanation as to when and why the deviations occur is highly desirable. A deep experimental study of the effects of detuning and the adiabaticity parameter could help finding the causes of the deviations. A numerical computation of the geometric phase for a system comprising five levels has recently be carried out by Marek Pechal. The results indicate that the higher levels cause a deviation from Berry's prediction which grows both with detuning Δ and with solid angle α. The computed deviation has the same sign as the observed deviation, however they do not match quantitatively. A perturbative expansion of the Hamiltonian describing a mutlilevel qubit exposed to drive gives results that are very similar to those obtained by the numerical computation.

5 Conclusion

The aim of this thesis was the measurement of Berry's phase in a transmon qubit coupled to a resonator. This goal was attained. Along the way, the pulses employed for qubit control were refined, leading to better agreement between Berry's theoretical predictions and the measured phases than in the first measurements. Various techniques, such as Ramsey-interferometry and the spin-echo procedure, were successfully applied in the course of this work.

After the first measurements of the geometric phase, it became apparent that it was necessary to use considerably slow and well-calibrated pulses. Otherwise, the precision attained in the measurements of Ref. [29] was out of reach. The energy-level structure of the transmon, notably the small anharmonicity, and the considerably shorter energy relaxation and dephasing times, may account for this. The experimentally obtained curves deviate from theory when the applied drive induces Rabi oscillations with approximately 40 MHz. In addition, the influence of the detuning applied during the pulse patterns and the role of the third level remain unquantified. Here, theoretical computations and numerical simulations show that the inclusion of higher levels causes the acquired phase to deviate increasingly from Berry's phase as the Rabi frequency increases. Even though the modelled deviations and the experimentally obtained deviations do not match quantitatively, the signs of the deviations agree. This is a starting point is for further investigations.

The Berry phase measurement is the starting point for a vast array of possible developments. One could examine the sensitivity of the geometric phase to artificial noise added to the path traced out by the qubit in parameter space to test the robustness of the phase and find a model describing the influence of fluctuations of various rates. The ability of manipulating two qubits dispersively coupled to a single resonator has been demonstrated [47], and this begs to implement a geometric two-qubit gate detuned from each other, as is proposed in Ref. [54]. Then, it is certainly worthwhile to explore the diverse generalisations of Berry's phase: what happens if we go without cyclicity, or without adiabaticity [33]? The latter idea is of particular interest for applications related to quantum computation. Indeed, this would allow to speed up gate operations and partially lessen the issues related to energy relaxation and dephasing while retaining the robustness.

A Conversion of drive amplitude

We seek how to convert the dimensionless amplitude $A \in [0,1]$ of the pulses generated in the pattern files into the real drive amplitude $\mathcal{E}$ (in angular frequency units). The time evolution of the qubit state is given by

$$|\psi(t)\rangle = \mathcal{T} \exp\left\{-\frac{\mathrm{i}}{\hbar}\int_0^t \mathrm{d}t'\, H(t')\right\}|\psi(0)\rangle.$$

We drive the qubit with radiation $\mathcal{E}(t)$ of frequency $\omega_d/2\pi$ on the $\mathcal{E}_x$-quadrature,

$$\mathcal{E}(t) = \mathcal{E}_x(t)\cos(\omega_d t).$$

From eqn. (2.18), we know that the Hamiltonian

$$H(t) = \hbar\mathcal{E}(t)\frac{\sigma_x}{2},$$

describes the interaction of the qubit with an resonant external radiation field in a frame rotating at ω_d. Thus, in this frame, the qubit state evolves according to

$$|\psi(t)\rangle = \exp\left\{-\mathrm{i}\int_0^t \mathrm{d}t'\, \mathcal{E}(t')\frac{\sigma_x}{2}\right\}|\psi(0)\rangle.$$

The time ordering operator has been omitted since there is only σ_x involved. Letting $|\psi(0)\rangle = |0\rangle$, and since $\exp\{\mathrm{i}p\sigma_x\} = \cos(p)\mathrm{id}_2 + \mathrm{i}\sin(p)\sigma_x$, we have

$$|\psi(t)\rangle = \cos\left(\frac{1}{2}\int_0^t \mathrm{d}t'\, s\mathcal{E}(t)\right) - \mathrm{i}\sin\left(\frac{1}{2}\int_0^t \mathrm{d}t'\, s\mathcal{E}(t)\right) \tag{A.1}$$

We now consider two cases.

Case 1.— We apply radiation with a square pulse envelope during the interval $[0,T]$, that is, $\mathcal{E}_x(t) = \mathcal{E}_0\chi_{[0,T]}$ with $\mathcal{E}_0 \in \mathbb{C}$. Then, from eqn. (A.1), we find

$$|\psi(T)\rangle = \cos\left(\frac{1}{2}\mathcal{E}_0 T\right)|0\rangle - \mathrm{i}\sin\left(\frac{1}{2}\mathcal{E}_0 T\right)|1\rangle. \tag{A.2}$$

If the duration of the pulse is $T = t_\pi = 2\pi/\mathcal{E}_0$, the qubit accumulates the phase π, and

$$|\psi(T)\rangle = \cos(\pi)|0\rangle - \mathrm{i}\sin(\pi)|1\rangle = -|0\rangle.$$

This corresponds to a 2π-pulse, since it maps $|0\rangle$ to $-|0\rangle$.

Case 2.— Now, we choose a pulse with an envelope having the shape of a truncated gaussian

$$\mathcal{E}_x(t) = \mathcal{E}_0 \rho(t) \chi_{[0,T]},$$

where $\rho(t)$ describes the truncated gaussian normalised to unit height. Then, eqn. (A.1) leads to

$$|\psi(T)\rangle = \cos\left(\frac{1}{2}\mathcal{E}_0 \int_0^T \mathrm{d}t\, \rho(t)\right)|0\rangle - \mathrm{i}\sin\left(\frac{1}{2}\mathcal{E}_0 \int_0^T \mathrm{d}t\, \rho(t)\right)|1\rangle.$$

and the requirement for obtaining a 2π-pulse is

$$\frac{1}{2}\mathcal{E}_0 \int_0^T \mathrm{d}t\, \rho(t) = \pi.$$

We now introduce s, the conversion factor permitting to transform the dimensionless amplitude $A(t)$ of the pulses generated using the AWG into drive amplitude in units of angular frequency, $\mathcal{E}_x(t) = sA(t)$. In our setup, the amplitude A_π corresponding to the π-pulse can determined by measuring the excited state population while sweeping the amplitude. So, writing $\mathcal{E}_0 = sA_\pi$ in the equation immediately above, we find that

$$s = \frac{2\pi}{A_\pi \int_0^T \mathrm{d}t\, \rho(t)}.$$

Bibliography

[1] P. W. Shor, *SIAM J. Sci. Statist. Comput.* **26**, 1484 (1997)

[2] L. K. Grover, 'A fast quantum mechanical algorithm for database search', in *STOC96: Proceedings of the twenty-eighth annual ACM symposium on Theory of computing*, 212 (New York: ACM Press, 1996)

[3] M. Nakahara, T. Ohmi, *Quantum Computing: From Linear Algebra to Physical Realizations* (Boca Raton: Taylor & Francis Group, 2008)

[4] H. Häffner, W. Hänsel et al., *Nature* **438**, 643 (2005)

[5] J. Majer, J. M. Chow et al., *Nature* **449**, 06184 (2007)

[6] J. Clarke and F. K. Wilhelm, *Nature* **453**, 1031 (2008)

[7] A. Blais, R.-S. Huang et al., *Phys.Rev. A* **69**, 062320 (2004)

[8] J. Koch, T. M. Yu et al., *Phys. Rev. A* **76**, 042319 (2007)

[9] P. W. Shor, *Phys. Rev. A* **52**, R2493 (1995)

[10] A. Anandan, Nature **360**, 307 (1992)

[11] J. A. Jones, V. Vedral et al., *Nature* **403**, 869 (2003)

[12] E. Sjöqvist, *Physics* **1**, 35 (2008)

[13] M. V. Berry, *Proc. R. Soc. Lond. A* **392**, 45 (1984)

[14] M. A. Nielsen, I. L. Chuang, *Quantum Computation and Quantum Information* (Cambridge: Cambridge University Press, 2007)

[15] S. M. Dutra, *Cavity Quantum Electrodynamics* (New York: John Wiley & Sons, 2005)

[16] S. Haroche and J.-M. Raimond, *Exploring the Quantum. Atoms, Cavities and Photons* (Oxford: Oxford University Press, 2008)

[17] `http://qist.lanl.gov/pdfs/qc_roadmap.pdf` (accessed on Feb. 12th, 2010)

[18] D. P. DiVincenzo, *Fortschr. Phys.* **48**, 771 (2000)

[19] E. Knill, 'Physics: Quantum computing', News and Views Q&A, *Nature* **463**, 441 (2010)

[20] E. T. Jaynes and F. W. Cummings, *Proc. IEEE*, **51**, 89 (1963)

[21] A. Wallraff, D. I. Schuster et al., *Nature* **431**, 162 (2004)

[22] D. I. Schuster, A. Wallraff et al., *Phys. Rev. Lett.* **94**, 123602 (2005)

[23] M. Tinkham, *Introduction to Superconductivity* (New York: Dover Publication, 2004)

[24] D. Vion, 'Josephson quantum bits based on a Cooper pair box', in *Quantum Entanglement and Information Processing (Les Houches Session LXXIX)*, eds J.-M. Raimond, J. Dalibard, and D. Estève, 521 (New York: Elsevier, 2003)

[25] A. A. Houck, J. Koch et al., *Quantum Inf. Process.* **8**, 105 (2009)

[26] J. A. Schreier, A. A. Houck et al., *Phys. Rev. B* **77**, 180502(R) (2008)

[27] C. J. Foot, *Atomic Physics* (Oxford: Oxford University Press, 2007)

[28] M. Fox, *Quantum Optics* (Oxford University Press, Oxford, 2007)

[29] P. J. Leek, J. M. Fink et al., *Science* **318**, 1889 (2007)

[30] S. Pancharatnam, *Proc. Indian Acad. Sci. A* **44**, 247-262 (1956)

[31] A. Messiah, *Quantenmechanik, Band 2* (Berlin: Walter de Gruyter, 1990)

[32] M. Nakahara, *Geometry, Topology and Physics* (Bristol: Institute of Physics Publishing 2003)

[33] Y. Aharonov and A. Anandan, Phys. Rev. Lett. **58**, 1593 (1987)

[34] J. Samuel and R. Bhandari, *Phys. Rev. Lett.* **60**, 2339 (1988)

[35] N. Manini, F. Pistolesi, *Phys. Rev. Lett.* **85**, 3067 (2000)

[36] B. Simon, *Phys. Rev. Lett.* **51**, 2167 (1983)

[37] A. Tomita and R. Y. Chiao, *Phys. Rev. Lett.* **57**, 938 (1986)

[38] T. Bitter and D. Dubbers, *Phys. Rev. Lett.* **59**, 251 (1987)

[39] R. Tycko, *Phys. Rev. Lett.* **58**, 2281-2284 (1987)

[40] D. Suter, K. T. Mueller and A. Pines, *Phys. Rev. Lett.* **60**, 1218 (1988)

[41] A. G. Wagh, V. C. Rakhecha, P. Fischer and A. Ioffe, Phys. Rev. Lett. **81**, 1992 (1998)

[42] M. Möttönen, J. J. Vartiainen and J. P. Pekola, *Phys. Rev. Lett.* **100** 177201 (2008)

[43] D. I. Schuster, A. A. Houck et al., *Nature* **445**, 05461 (2007)

[44] M. Göppl, A. Fragner et al., *J. Appl. Phys.* **104**, 113904 (2008)

[45] R. N. Simons, *Coplanar Waveguide Circuits, Components, and Systems* (New York: John Wiley & Sons, 2001)

[46] D. M. Pozar, *Microwave Engineering* (New York: John Wiley & Sons, 2005)

[47] P. J. Leek, S. Filipp et al., *Phys. Rev. B* **79**, 180511 (2009)

[48] C. Lang, *Read-Out Strategies for Multi-Qubit States in Circuit Quantum Electrodynamics*, Diploma thesis (Ludwigs-Maximilans-Universität München, 2009)

[49] R. Bianchetti, S. Filipp et al., *Phys. Rev. A* **80**, 043840 (2009)

[50] F. Motzoi, J. M. Gambetta, P. Rebentrost, and F. K. Wilhelm, *Phys. Rev. Lett.* **103**, 110501 (2009)

[51] D. Vion, A. Aassime et al., *Fortschr. Phys.* **51**, 462 (2003)

[52] A. Abragam, *Principles of Nuclear Magnetism* (Oxford: Oxford University Press, 1961)

[53] J. M. Fink, *Single Qubit Control and Observation of Berry's Phase in a Superconducting Quantum Circuit*, Diploma thesis (Universität Wien, 2007)

[54] A. Blais, J. Gambetta et al., *Phys. Rev. A* **75**, 032329 (2007)

Acknowledgements

First and foremost, I would like to express my gratitude to Prof. Dr. Andreas Wallraff, who gave me the opportunity to write my thesis in his laboratory, the Quantum Device Lab at ETH Zurich and provided me with valuable inputs all along the elaboration of this work.

My thanks also go to Dr. Stefan Filipp, who supervised my thesis and explained to me a great many things, be it theoretical matters, the intricacies of the measurement setup or the quirks of *Mathematica*. I am also indebted to him for his astute comments on the experimental results I could not make head or tail of, and for his inventiveness—without his advice, making headway would have been a formidable task.

Whenever I hit a snag with the heavy engineering machinery in the basement, or was unable to cater to *LabVIEW*'s every whim, I knew that my call upstairs would be answered either by Romeo Bianchetti and Matthias Baur, who were working on the same setup and know its every nook and cranny. Thank you for your patient and unremitting support. I owe many thanks to Christian Lang, who automatised the calibration of the mixer of the input signal—his work has saved me countless hours of terminal boredom.

I am also indebted to Johannes M. Fink and Dr. Peter Leek, who have, some two years ago, carried out the first measurement of geometric phases in a split-CPB. Thank you for letting me draw on your ideal and material experience.

Then, special thanks go to Arjan van Loo, with whom I shared the office along with Stefan Filipp, for his virtually inexhaustible wealth of conversational topics, be it wŭshù, jazz, Japanese anime series or simply down-to-earth physics.

Finally, I would like to thank the other members of the team, Deniz Bozyigit, Christopher Eichler, Tobias Frey, Gabriel Puebla-Hellmann, Jonas Mlynek and Lars Steffen, as well as the other staff members.